



Article

# Novel Pt-Ag<sub>3</sub>PO<sub>4</sub>/CdS/Chitosan Nanocomposite with Enhanced Photocatalytic and Biological Activities

Mahsa Kiani <sup>1</sup>, Mojtaba Bagherzadeh <sup>1,\*</sup>, Reyhaneh Kaveh <sup>1</sup>, Navid Rabiee <sup>1</sup> ,  
Yousef Fatahi <sup>2,3,4</sup> , Rassoul Dinarvand <sup>2,3</sup> , Ho Won Jang <sup>5</sup> ,  
Mohammadreza Shokouhimehr <sup>5,\*</sup> and Rajender S. Varma <sup>6,\*</sup>

- <sup>1</sup> Department of Chemistry, Sharif University of Technology, P.O. Box 11155-3516, Tehran 14155-6451, Iran; mahsa.kiani88@gmail.com (M.K.); reyhanehkaveh@yahoo.com (R.K.); nrabiee94@gmail.com (N.R.)  
<sup>2</sup> Department of Pharmaceutical Nanotechnology, Faculty of Pharmacy, Tehran University of Medical Sciences, Tehran 14155-6451, Iran; youseffatahi@gmail.com (Y.F.); dinarvand@tums.ac.ir (R.D.)  
<sup>3</sup> Nanotechnology Research Center, Faculty of Pharmacy, Tehran University of Medical Sciences, Tehran 14155-6451, Iran  
<sup>4</sup> Universal Scientific Education and Research Network (USERN), Tehran 15875-4413, Iran  
<sup>5</sup> Department of Materials Science and Engineering, Research Institute of Advanced Materials, Seoul National University, Seoul 08826, Korea; hwjang@snu.ac.kr  
<sup>6</sup> Regional Center of Advanced Technologies and Materials, Palacky University, Šlechtitelů 27, 78371 Olomouc, Czech Republic  
\* Correspondence: bagherzadeh@sharif.edu (M.B.); mrsh2@snu.ac.kr (M.S.); varma.rajender@epa.gov (R.S.V.)

Received: 14 October 2020; Accepted: 20 November 2020; Published: 23 November 2020



**Abstract:** Decorating photocatalysts with noble metal nanoparticles (e.g., Pt) often increases the catalysts' photocatalytic activity and biomedical properties. Here, a simple and inexpensive method has been developed to prepare a Pt-Ag<sub>3</sub>PO<sub>4</sub>/CdS/chitosan composite, which was characterized and used for the visible light-induced photocatalytic and antibacterial studies. This synthesized composite showed superior photocatalytic activity for methylene blue degradation as a hazardous pollutant (the maximum dye degradation was observed in 90 min of treatment) and killing of Gram positive bacterial (*Staphylococcus aureus* and *Bacillus cereus*) as well as Gram negative bacteria (*Klebsiella pneumoniae*, *Salmonella typhimurium*, *Escherichia coli*, and *Pseudomonas aeruginosa*) under visible light irradiation. The antibacterial activity of CdS, CdS/Ag<sub>3</sub>PO<sub>4</sub>, and Pt-Ag<sub>3</sub>PO<sub>4</sub>/CdS/chitosan against *E. coli*, *Pseudomonas aeruginosa*, *Salmonella typhimurium*, *Klebsiella pneumoniae*, *Staphylococcus aureus*, and *Bacillus cereus* showed the zone of inhibition (mm) under visible light and under dark conditions at a concentration of 20 µg mL<sup>-1</sup>. Furthermore, the cell viability of the CdS/chitosan, Ag<sub>3</sub>PO<sub>4</sub>, Ag<sub>3</sub>PO<sub>4</sub>/CdS/chitosan, and Pt-Ag<sub>3</sub>PO<sub>4</sub>/CdS/chitosan were investigated on the human embryonic kidney 293 cells (HEK-293), Henrietta Lacks (HeLa), human liver cancer cell line (HepG2), and pheochromocytoma (PC12) cell lines. In addition, the results indicated that the photodegradation rate for Pt-Ag<sub>3</sub>PO<sub>4</sub>/CdS/chitosan is 3.53 times higher than that of CdS and 1.73 times higher than that of the CdS/Ag<sub>3</sub>PO<sub>4</sub> composite. Moreover, Pt-Ag<sub>3</sub>PO<sub>4</sub>/CdS/chitosan with an optimal amount of CdS killed large areas of different bacteria and different cells separately in a shorter time period under visible-light irradiation, which shows significantly higher efficiency than pure CdS and other CdS/Ag<sub>3</sub>PO<sub>4</sub> composites. The superb performances of this composite are attributed to its privileged properties, such as retarded recombination of photoinduced electron/hole pairs and a large specific surface area, making Pt-Ag<sub>3</sub>PO<sub>4</sub>/CdS/chitosan a valuable composite that can be deployed for a range of important applications, such as visible light-induced photocatalysis and antibacterial activity.

**Keywords:** Pt-Ag<sub>3</sub>PO<sub>4</sub>/CdS/chitosan; photocatalytic activity; antibacterial activity; cytotoxicity; visible light

## 1. Introduction

Scientists have lately focused on antibacterial finishing on different types of textile materials because of their importance in environmental pollutions. In this case, using nanomaterials with improved antibacterial and cellular properties has been raised. The deployment of some transition metal nanoparticles (NPs) offers a practical approach in improving the potential biological properties. Silver is an excellent antibacterial agent because of its chemical and electronic structure, which enables it to penetrate the bacteria's wall and kill them; the half maximal inhibitory concentration ( $IC_{50}$ ) of silver NPs (AgNPs) is lower than other transition metal NPs, which makes it an appropriate candidate for different biomedical applications [1–5].

Many of the medicinal residues in water, sewage, and pigments in the water line are considered as severe threats to human health [6,7]. Environmental inorganic and organic pollution, created by industries, is a primary concern for human-race and public health because of contaminated foods and waters. Consequently, there is a necessity for industrial-active components and nanomaterials with low cytotoxicity towards different cell lines, for removing the presence of pollutants via dual-functioning nanomaterials [8,9]. There are several potentially toxic and often drug-resistant microorganisms in the environment. For example, species such as *Methicillin-resistant Staphylococcus aureus* (MRSA) are highly prevalent in hospital and municipal wastewater [10]. Several strains of *Escherichia coli*, including problematic strains that are resistant to known drugs, are found in the water [11,12]. Other microorganisms such as *Pseudomonas aeruginosa* and *Salmonella typhimurium* were also found in the river and coastal waters. Thus, immediate steps need to be taken for the development of highly active dual-functional nanomaterials with the potential of working as an antibacterial agent as well as pollutant adsorbents [13].

Pollution from organic contaminants is one of the significant challenges faced by the global society. Estimates indicate that over ten thousand different dyes are used industrially, and over  $7 \times 10^5$  tons of synthetic dyes are produced all around the world every year. There are a significant number of synthetic dyestuffs in the raw water without any treatment or industrial sewage, which consequently has a considerable impact on the *global environment* [14–17].

Recently, the field of heterogeneous photocatalysis has expanded rapidly as an efficient way to reduce both the microbial contamination and organic pollution in wastewaters at the same time. The photocatalyst, as the semiconductor material, has two energy bands: the valence band (VB), which is the highest energy band with electrons, and the conduction band (CB), which is the lowest energy band without electrons. In addition, the forbidden energy gap between these two bands is called bandgap energy ( $E_g$ ) [18–20]. In the photocatalytic process, the exposure of a photocatalyst to light excites it by supplying its band gap energy; consequently, an electron ( $e^-$ ) is promoted from the VB to CB, leaving a hole ( $h^+$ ) behind. The photoinduced couple ( $e^-/h^+$ ) can reduce or oxidize a contaminant adsorbed on the photocatalyst surface [21–24]. Furthermore, the nanocomposite can have different application, such as antibacterial and photocatalytic activity. The typical reaction that instigates the antibacterial action is based on the redox reactions on the surface of the material, which lead to the generation of reactive oxygen species (ROS) and react with the cell walls of the bacterial strain [25–27].

Silver orthophosphate ( $Ag_3PO_4$ ), a renowned narrow bandgap semiconductor, has attracted intense research interest thanks to its significant photocatalytic activity [28–30]. However, the stability of the synthesized nanomaterials depends on the solubility in different solutions, specifically water [31–33]. In addition,  $Ag_3PO_4$  suffers from photo corrosion of  $Ag^+$  into  $Ag^0$  in the process of photocatalytic assay; therefore, composites should be synthesized to limit these detrimental effects [33]. In this manner, two or more different semiconductors could form a novel  $Ag_3PO_4$  nanocomposite with an optimized and tunable band energies to facilitate the photocatalytic activities as well as reduce the recombination rate of  $e^-/h^+$  pairs. Yao et al. prepared  $Ag_3PO_4/TiO_2$  visible-light composite by depositing  $Ag_3PO_4$  NPs onto the surface of  $TiO_2$  (P-25) [34,35]; this visible light photocatalyst displayed increased activity and is much more stable than pure  $Ag_3PO_4$  NPs as it is related to the  $e^-/h^+$  efficient separation and

the high surface area of the  $\text{Ag}_3\text{PO}_4/\text{TiO}_2$  photocatalyst. At the same time, the increased stability is attributed to the chemical adsorption of  $\text{Ag}^+$  cations in  $\text{Ag}_3\text{PO}_4$  and anions of  $\text{O}^-$  in  $\text{TiO}_2$  [34,36].

Bi et al. have prepared the  $\text{AgX}/\text{Ag}_3\text{PO}_4$  ( $X = \text{Cl}, \text{Br}, \text{I}$ ) composite via the in situ ion-exchange method, which showed higher photocatalytic activity compared with pure  $\text{Ag}_3\text{PO}_4$  [37,38]. Similarly,  $\text{Ag}_3\text{PO}_4$ -based composite photocatalysts including  $\text{MFe}_2\text{O}_4/\text{Ag}_3\text{PO}_4$  ( $M = \text{Ca}, \text{Mg}$ ) [32],  $\text{In}(\text{OH})_3/\text{Ag}_3\text{PO}_4$  [39],  $\text{Ag}@\text{Ag}_2\text{S}/\text{Ag}_3\text{PO}_4$  [40], and so on have superior photocatalytic performance than single  $\text{Ag}_3\text{PO}_4$ .

Cadmium sulfide (CdS) is considered as one of the most promising semiconductors for photocatalytic process, because of its superior ability in absorbing visible light [41,42]. However, these NPs have poor ability in separating the photoinduced  $e^-/h^+$  pairs, thus limiting their photocatalytic efficiency. A strategy for decreasing the recombination rate of  $e^-/h^+$  pairs on CdS is to combine it with other semiconductors such as  $\text{NiFe}_2\text{O}_4$  [43],  $\text{ZnO}$  [44], and  $\text{Ag}_3\text{PO}_4$  [45].

Synthesis of multifunctional nanostructured materials has garnered intense attention thanks to their improved physical and chemical properties in electronics, antibacterial, optics, and catalysis. Cadmium sulfide (CdS) is an important II-VI semiconductor with a direct band gap energy of 2.42 eV and has significant applications in dye-sensitized solar cells [46], fluorescence probes [47], displays, photocatalysts [48], and laser light emitting diodes and optoelectronic devices [49] owing to absorption of most of the visible light in the solar spectrum. As for photocatalysts, a high surface area can be the most important factor in certain photocatalytic reactions as they occur on the surface of catalyst in contact with substrates, where reactant molecules must be first adsorbed by the photocatalyst [50].

Kyung Jo et al. prepared the nanocomposite of  $\text{CdS}/\text{Ag}_3\text{PO}_4$  and reported its higher visible light photocatalytic activity relative to the pure  $\text{Ag}_3\text{PO}_4$  and CdS nanocrystals, presumably because of the extended life-time of photogenerated  $e^-/h^+$  pairs and the enhancement of visible light absorption [51]. Chava et al. fabricated the heteronanostructure of  $\text{CdS}/\text{Ag}_3\text{PO}_4$  via solvothermal followed by the chemical reaction method. The photocatalytic hydrogen production rate of this heteronanostructure was evaluated using an aqueous solution containing methanol under visible light illumination; the heteronanostructure exhibited a higher photocatalytic hydrogen evolution rate than that of CdS under visible light irradiation. This showed that the specially formed heterojunctions between CdS and  $\text{Ag}_3\text{PO}_4$  favor the separation of photoinduced electron-hole pairs, which promoted the photocatalytic hydrogen evolution rate [52]. Mirsalari et al. synthesized NPs of CdS and  $\text{Ag}_3\text{PO}_4$  by the sol-gel/mechanicochemical method. The increased photocatalytic activity of  $\text{CdS}/\text{Ag}_3\text{PO}_4$  nanocomposite towards MB and its lower photoluminescence (PL) intensity can be ascribed to the faster charge carrier's transfer in the coupled system relative to the individual CdS and  $\text{Ag}_3\text{PO}_4$  precursors [53].

Besides, decorating the prepared photocatalysts with noble metal NPs, such as Pt, is an ideal way to increase the photocatalytic activity and photocatalytic antibacterial properties. In fact, under illumination, the photoinduced electrons in the semiconductor CB can be efficiently directed to the metal NPs attached on the surface, and they can act as sinks for photogenerated electrons. This effect retards the recombination rate of photogenerated electron and hole pairs and prolongs the lifetime of carriers [54].

Chitosan, as an important nature-derived polysaccharide, bearing active functional groups including hydroxyl ( $-\text{OH}$ ) and reactive amino ( $-\text{NH}_2$ ) groups, has found extensive applications thanks to its low toxicity, significant biocompatibility, adequate water permeability, and high mechanical strength [55–57]. Based on the well-established studies, chitosan is commonly used as an adsorbent in environmental science. The functional groups of chitosan could provide plentiful chelation sites for organic pollutants. In the domain of catalysis, chitosan has been selected as a carrier to synthesize composite catalysts for advanced oxidation processes [58,59].

Cao et al. reported the preparation of  $\text{Ag}_3\text{PO}_4/\text{chitosan}/\text{CdS}$  nanocomposite via the in situ growth approach and investigated the photocatalytic activity of this photocatalyst by the decolorization behavior of methyl orange under visible-light illumination [33].

Herein, for the first time, we have synthesized a novel  $\text{Pt}-\text{Ag}_3\text{PO}_4/\text{CdS}/\text{chitosan}$  nanocomposite and explored its potential photophysical and biological properties. The presence of Pt NPs in the

nanocomposite of Pt-Ag<sub>3</sub>PO<sub>4</sub>/CdS/chitosan can play an important role in the photodegradation process and delays the recombination rate of e<sup>-</sup>/h<sup>+</sup> pairs. In fact, these NPs with large work functions are used as the electron sinks to trap the photoinduced electrons from the CB of Ag<sub>3</sub>PO<sub>4</sub>, thus enhancing the lifetime of the photoinduced charge carriers. Moreover, these NPs can function as co-catalysts offering the active sites for reduction reactions [60–62]. Consequently, the introduction of Pt NPs into the Ag<sub>3</sub>PO<sub>4</sub>/CdS/chitosan nanocomposite has shown significant positive effect on the enhancement of photocatalytic performance.

Interestingly, Prabu et al. prepared the metal colloidal solutions of Pt and Pt-Pd. Antibacterial activity of polyaniline/Pt nanocomposite has been studied with different bacterial strains for food packaging and medical devices, wherein polyaniline has significant antibacterial activity against *E. coli* and *S. aureus* under dark and visible light conditions. Polyaniline, dissolved in dimethyl sulfoxide at different concentrations, displayed antibacterial property against various Gram-positive and Gram-negative bacterial strains and polyaniline incorporated with metal NPs (Pt) also reportedly exhibited enhanced biological activity [63]. The photocatalytic performance of Pt-Ag<sub>3</sub>PO<sub>4</sub>/CdS/chitosan nanocomposite was gauged by photodegradation of methylene blue (MB) as a dangerous pigment under visible light irradiation. Furthermore, extensive antibacterial, antioxidant, and cellular viability studies of this novel 3D nanocomposite were undertaken.

## 2. Experimental

### 2.1. Materials

Chitosan (with the de-acetylation degree of about 85%), extracted from the shells of a shrimp, and K<sub>2</sub>PtCl<sub>2</sub> were obtained from Sigma-Aldrich, GmbH, Germany. The silver nitrate (AgNO<sub>3</sub>), sodium phosphate monobasic (NaH<sub>2</sub>PO<sub>4</sub>), potassium chloride (KCl), cadmium acetate Cd(CH<sub>3</sub>COO)<sub>2</sub>·2H<sub>2</sub>O, ammonia solution, and MB (C<sub>16</sub>H<sub>18</sub>N<sub>3</sub>S) were procured from Merck, GmbH, Germany. Other chemicals and solvents such as dimethyl sulfoxide (CH<sub>3</sub>)<sub>2</sub>SO, ethanol (C<sub>2</sub>H<sub>6</sub>O), and distilled water were of analytical grade and were used as received.

### 2.2. Characterization Methods

Room temperature Fourier transform infrared (FTIR) spectra of CdS, chitosan, and Pt-Ag<sub>3</sub>PO<sub>4</sub>/CdS/chitosan nanocomposite were collected with a Bruker Tensor 27 spectrometer (Ettlingen, Germany) using a KBr pellet for sample preparation. The structure of samples was identified by X-ray diffraction (XRD) with an XPERT-PRO diffractometer using Cu *Kα* radiation. Ultraviolet-visible (UV-vis) diffuse reflectance spectra (DRS) were obtained on an Avaspec-2048-TEC UV-vis-near-infrared (NIR) (Avantes, Louisville, CO, USA) spectrometer with barium sulfate (BaSO<sub>4</sub>) powder as the internal standard in order to achieve the optical properties of the samples over a wavelength range of 200–800 nm. All binding energies were determined by this method. An ASAP 2020 surface area analyzer (Micromeritics, GmbH, Germany) was used to carry out the Brunauer-Emmett-Teller (BET) surface area analysis. The morphology of the prepared samples was observed by field emission scanning electron microscope (FESEM, TESCAN MIRA II, TESCAN, Brno, Czech Republic).

The bacteria were spread on nutrient agar plate and cultured at 37 °C for 24 h. A concentration of bacteria equivalent to 10<sup>5</sup> CFU/mL (colony forming units per milliliter) was prepared by harvesting bacteria in NaCl solution and then the inoculum concentration was determined by McFarland standard and confirmed by serial dilutions.

### 2.3. Synthesis Steps

#### 2.3.1. Synthesis of CdS

For this aim, 2 mmol of Cd(OAc)<sub>2</sub> was dissolved in 40 mL of dimethyl sulfoxide (DMSO), the mixture was stirred using an ultrasonic bath for 2 h, and the sonicated solution was poured into a

150 mL autoclave (Teflon lined stainless steel) and kept at 130 °C for 28 h. After that, the autoclave was cooled to room temperature and the product (yellow powder) was obtained. The resulting CdS NPs were filtered and washed several times using acetone and ethanol and dried at 60 °C.

### 2.3.2. Synthesis of CdS/Ag<sub>3</sub>PO<sub>4</sub> Nanocomposite with a Mass Ratio of 3:7

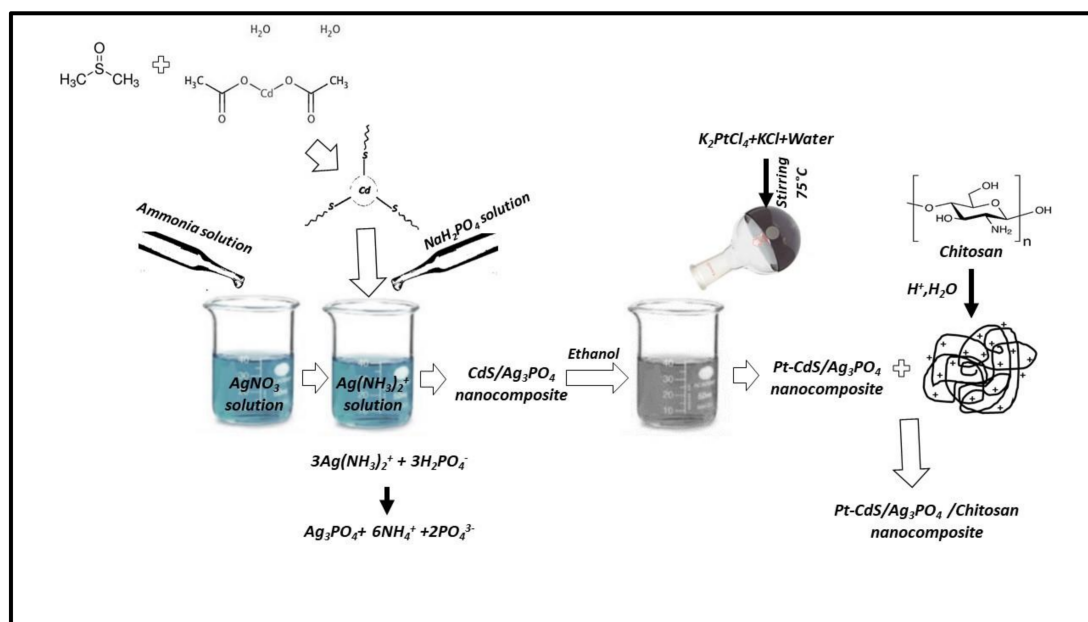
Briefly, AgNO<sub>3</sub> (3 mmol) was dissolved in distilled water (40 mL) and a 10 mL aqueous ammonia (1.0 M) was poured into the first solution slowly. Next, CdS (0.38 g) was introduced to the mixture and stirred for about two hours. NaH<sub>2</sub>PO<sub>4</sub> (0.1 M, 20 mL) was poured into the mixture dropwise and stirred again for one more hour. The obtained precipitates were washed for several times with deionized water and dried at 70 °C. The product CdS/Ag<sub>3</sub>PO<sub>4</sub> was obtained as a black solid.

### 2.3.3. Synthesis of Pt-Ag<sub>3</sub>PO<sub>4</sub>/CdS Nanocomposite

In this step, 0.4 mmol of K<sub>2</sub>PtCl<sub>6</sub> as well as 9 mmol of KCl were added to 10 mL deionized water in a 100 mL round-bottom flask while stirring constantly. This flask was also heated at 75 °C to completely dissolve the KCl. After cooling the solution to about room temperature, this prepared solution was added to CdS/Ag<sub>3</sub>PO<sub>4</sub> (450 mg in 25 mL ethanol) slowly. Finally, the obtained suspension was stirred for 4 h and filtered under reduced pressure [64].

### 2.3.4. Synthesis of Pt-Ag<sub>3</sub>PO<sub>4</sub>/CdS/Chitosan Nanocomposite with a Mass Ratio of 3:2

Briefly, chitosan (0.15 g) was dissolved using acetic acid (1.5%, 30 mL, *v/v*); then, an exact amount of Pt-Ag<sub>3</sub>PO<sub>4</sub>/CdS powder (0.225 g) was added to the solution and sonicated for 2 h. The obtained mixture was filtered using a reduced pressure system and washed several times with methanol and deionized water. The product Pt-Ag<sub>3</sub>PO<sub>4</sub>/CdS/chitosan was obtained as a black solid. The synthesis process for the Pt-Ag<sub>3</sub>PO<sub>4</sub>/CdS/chitosan nanocomposite is depicted in Scheme 1.



**Scheme 1.** The synthesis process for the Pt-Ag<sub>3</sub>PO<sub>4</sub>/CdS/chitosan nanocomposite.

## 2.4. Photocatalytic Degradation of MB

The photocatalytic ability of the synthesized nanocomposite was evaluated by observation of the MB degradation. For the visible light source, NVSWE21AT was employed, and in all of the measurements, the distance between the light source and MB solution was kept at 3 cm. Figure S1 depicts the emission wavelength of the used NVSWE21AT light source. For each test, 0.01 g of the

prepared photocatalyst was added to the 40 mL of MB aqueous solutions with a concentration of  $10^{-5}$  mol L $^{-1}$ . Finally, the MB concentration was calculated via monitoring the absorbance spectra at 668 nm. The photocatalytic performance was investigated through the degradation rate ( $X$ ) of MB obtained from the below equation:

$$X(\%) = [(C_0 - C_t)/C_0] \times 100 \quad (1)$$

where  $X(\%)$  is the degradation rate of MB at time  $t$  minutes, and  $C_0$  and  $C_t$  are MB concentrations at time 0 and  $t$  minutes, respectively.

After the reaction in each run, the catalyst was collected and dried at 95 °C. Additionally, the experiment for trapping the free radical was conducted to investigate the exact role of reactive species. In this case, *tert*-butyl alcohol (t-BuOH) was selected as the scavenger of hydroxyl radical ( $\bullet$ OH), the scavenger of superoxide radical ( $O_2^{\bullet-}$ ) was chosen to be benzoquinone (BZQ), and the scavenger of hole ( $h^+$ ) was selected to be KI; one mM of each scavenger species was added to the mixture in each test.

### 2.5. Antibacterial Test under Visible Light and Dark Conditions

The antibacterial evaluation of Pt-Ag $_3$ PO $_4$ /CdS/chitosan nanocomposite, CdS, and CdS/Ag $_3$ PO $_4$  was investigated by the disk-diffusion method. Six bacterial strains named Gram-negative bacteria (*Klebsiella pneumonia*, *Salmonella typhimurium*, *Pseudomonas aeruginosa*, and *Escherichia coli*) and Gram-positive bacterial (*Bacillus cereus* and *Staphylococcus aureus*) were selected for this assay. The surface of Muller Hinton agar (MHA) was injected via the bacteria by rushing the swab, and afterward, disks were soaked in 0–20  $\mu$ g/mL of Pt-Ag $_3$ PO $_4$ /CdS/chitosan solution that was positioned on the injected agars [65,66]. To ensure antibacterial activity of the final material, two precursors, CdS and CdS/Ag $_3$ PO $_4$ , were also tested; they displayed lower antibacterial activity compared with the final material. The standard antibiotic *Penicillin* and *Gentamicin* were used as positive controls and distilled water as negative control in each replicate. The plates were incubated at 37 °C for 2 h under visible light and the dark environment for assessment of the antibacterial activity [67,68]; irradiation was performed under visible light (natural indoor light during the day and 100 W fluorescent lamps overnight) for a certain time.

### 2.6. MTT Assay

Before cell culture, samples were sterilized using ultraviolet exposure followed by washing with ethanol (75%) and phosphate buffer saline (PBS) solution. Cytocompatibility assessment was performed using MTT (3-[4,5-dimethylthiazol-2-yl]-2,5-diphenyltetrazolium bromide) (MTT, Sigma, GmbH, Germany) colorimetric assay at 24 and 48 h. PC12 cells (ATCC CRL-1721<sup>TM</sup>), HEK-293(ATCC CRL-1721<sup>TM</sup>), HeLa (ATCC CCL-2), and HepG2 (ATCC HB 8065) were used for this experiment. Briefly,  $1 \times 10^5$  cells/well were cultured on the synthesized nanocomposite substrate in Dulbecco's modified Eagle's medium (DMEM, Gibco, Thermo Fisher Scientific, GmbH, Germany) containing 100 IU/mL *penicillin*, 100 IU/mL streptomycin (Invitrogen), and 10% fetal bovine serum (FBS; Gibco, Germany) and incubated at 37 °C at 5% CO $_2$ . At each time point, 100  $\mu$ L of MTT solution (5 mg/mL in PBS) was added to each well. After 4 h incubation, the medium was removed and the formazone precipitates were dissolved in dimethyl sulfoxide (DMSO; Sigma-Aldrich). The optical absorbance was measured at 570 nm using a microplate Elisa reader (ELX808, BioTek, Bad Friedrichshall, Germany). At least three samples were averaged to calculate each time point.

## 3. Results and Discussion

### 3.1. Characterizations

The Inductively coupled plasma atomic emission spectroscopy (ICP-AES) result showed that the loading of Pt was 1.19% *w/w* Pt. Figure 1 depicts the FTIR spectra of raw CdS, chitosan, and Pt-Ag $_3$ PO $_4$ /CdS/chitosan nanocomposites in the range 4000–400 cm $^{-1}$ . The FTIR spectrum of CdS showed four characteristic peaks at 3422, 1620, 1400, and 1100 cm $^{-1}$ , respectively. The peaks at 3422 and 1620 cm $^{-1}$

are related to the adsorbed water molecules on the surface of CdS NPs. The FTIR characteristic peaks at 1400 and 1100  $\text{cm}^{-1}$  are attributed to the Cd-S band [69]. As observed in the FTIR spectrum of Pt- $\text{Ag}_3\text{PO}_4/\text{CdS}/\text{chitosan}$  nanocomposite, the peak of O-H and N-H stretching vibration at 3425  $\text{cm}^{-1}$  in spectrum of chitosan shifted to 3398  $\text{cm}^{-1}$ , and the peaks of  $-\text{NH}_2$  and  $-\text{OH}$  at 1602  $\text{cm}^{-1}$  and 1421  $\text{cm}^{-1}$  moved to 1574  $\text{cm}^{-1}$  and 1404  $\text{cm}^{-1}$ , respectively. These results showed that both the hydroxyl group and the amino group were engaged in the coordination reaction [70]. In addition, the peak of Cd-S bond vibration at 1100  $\text{cm}^{-1}$  in the spectrum of CdS became broad and weak and moved to 1020  $\text{cm}^{-1}$  in Pt- $\text{Ag}_3\text{PO}_4/\text{CdS}/\text{chitosan}$ . This result provides more evidence for the fusion of CdS NPs to other NPs in the prepared nanocomposite. Figure S2 shows the FTIR spectrum of  $\text{Ag}_3\text{PO}_4$  NPs, which is based on our previously published study [32]. The band at 3176  $\text{cm}^{-1}$  is attributed to the O-H stretching of water molecules. The sharp peak at 1388  $\text{cm}^{-1}$  is related to the antisymmetric stretching mode of the  $\text{PO}_4^{3-}$  group, whereas the corresponding symmetric vibration mode is found at 763  $\text{cm}^{-1}$ . The asymmetric stretching vibration of P-O bonds is found at 1020  $\text{cm}^{-1}$ , whereas the peak at 547  $\text{cm}^{-1}$  is attributed to the asymmetric bending mode of P-O bonds [71].

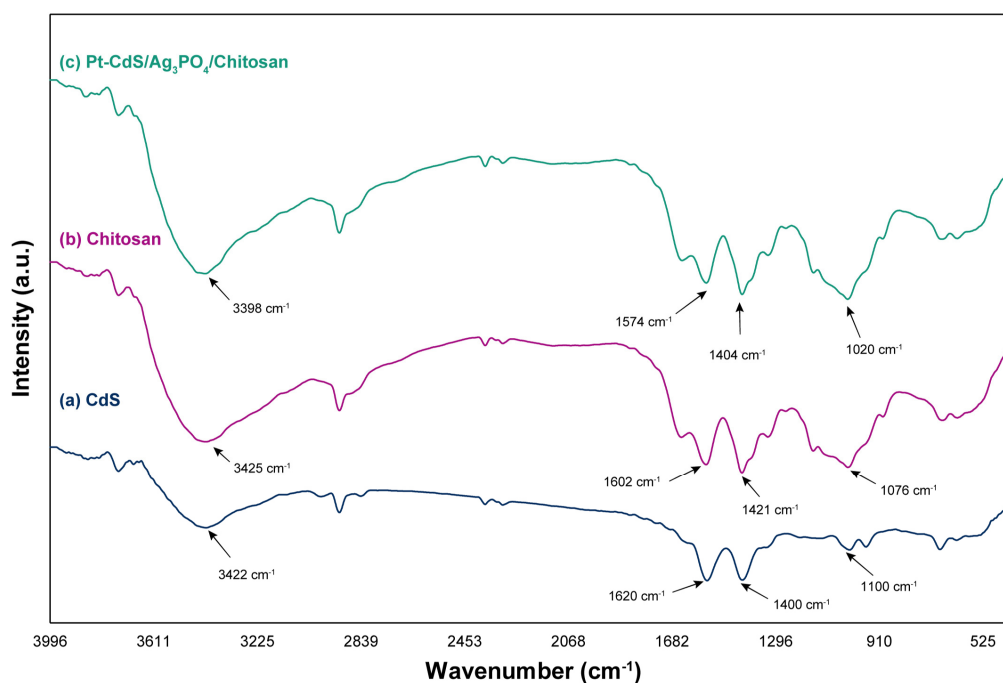


**Figure 1.** Fourier transform infrared (FTIR) spectra of (a) cadmium sulfide (CdS), (b) chitosan, and (c) Pt- $\text{Ag}_3\text{PO}_4/\text{CdS}/\text{chitosan}$  (the spectrum of  $\text{Ag}_3\text{PO}_4$  was reproduced with permission from [32]; Copyright John Wiley & Sons, 2018).

XRD patterns for CdS, CdS/ $\text{Ag}_3\text{PO}_4$ , and Pt- $\text{Ag}_3\text{PO}_4/\text{CdS}/\text{chitosan}$  nanocomposite are depicted in Figure 2. The XRD pattern of pure CdS showed characterization peaks at 26.6°, 44°, and 51.9°, which were related to the (111), (220), and (311) planes, respectively (JCPDS 89-0440). In the XRD pattern of Pt- $\text{Ag}_3\text{PO}_4/\text{CdS}/\text{chitosan}$  in Figure 2, the diffraction peak at ~27° of CdS and the peaks at 32.2°, 33.9°, 36.9°, 43.5°, 46°, 54.8°, and 57°, assigned to the (200), (210), (211), (220), (310), (320), and (321) planes of  $\text{Ag}_3\text{PO}_4$ , respectively, were vividly observed. Because of the low Pt loading on CdS/ $\text{Ag}_3\text{PO}_4/\text{chitosan}$  nanocomposite, no Pt diffraction peaks were detected [43,72]. XRD patterns for  $\text{Ag}_3\text{PO}_4$  are shown in Figure S3. All diffraction peaks can be indexed to  $\text{Ag}_3\text{PO}_4$  (JCPDS NO. 6-0505).

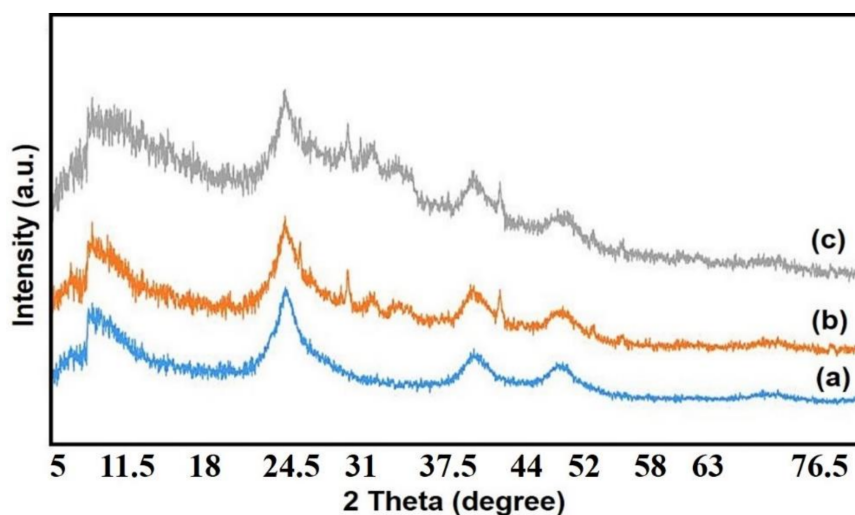


**Figure 2.** X-ray diffraction (XRD) patterns of (a) CdS, (b) Pt-Ag<sub>3</sub>PO<sub>4</sub>/CdS/chitosan, and (c) CdS/Ag<sub>3</sub>PO<sub>4</sub>.

The optical properties of the synthesized samples were studied by the diffuse reflectance spectra (DRS). Figure 3a depicts the DRS of CdS, Ag<sub>3</sub>PO<sub>4</sub>, and Pt-Ag<sub>3</sub>PO<sub>4</sub>/CdS/chitosan samples with clear red shift and intense absorptions in the wavelength ranging from 400 to 800 nm. Figure 3b shows the corresponding first derivative of the aforementioned spectra. The absorption edge of the synthesized samples can be obtained from the peaks on the first derivative spectra. Based on the attained results, CdS and Ag<sub>3</sub>PO<sub>4</sub> have an absorption edge at 491 and 644 nm, respectively. According to the absorption edge, the band gap energy ( $E_g$ ) of CdS and Ag<sub>3</sub>PO<sub>4</sub> is calculated to be 2.52 and 1.92 eV, respectively. It should be mentioned that the  $E_g$  of these two samples are slightly different from standard values, which may be related to the different preparative conditions of the process [32,73]. The absorption edge of Pt-Ag<sub>3</sub>PO<sub>4</sub>/CdS/chitosan is located at 773 nm, implying a band gap energy of 1.60 eV. Therefore, the Pt-Ag<sub>3</sub>PO<sub>4</sub>/CdS/chitosan nanocomposite could have a good photocatalytic performance under visible light irradiation [74–78].

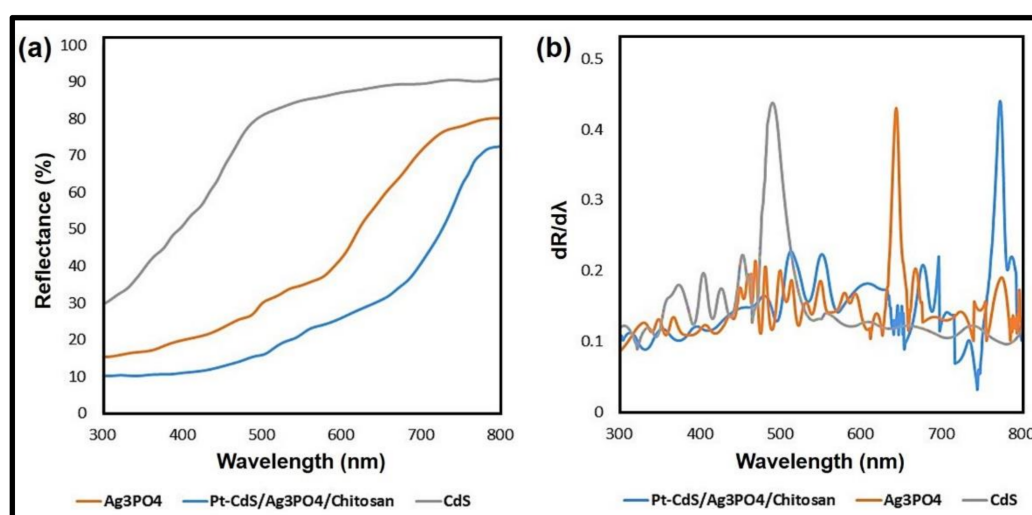


**Figure 3.** (a) The UV-vis diffuse reflectance spectra (DRS) of CdS, Ag<sub>3</sub>PO<sub>4</sub>, and Pt-Ag<sub>3</sub>PO<sub>4</sub>/CdS/chitosan; (b) the corresponding first derivative spectra.

The surface area of the prepared samples was investigated by BET analysis (Figure 4a–c). According to the BET results, the surface area values were found to be 10.796 m<sup>2</sup>/g, 21 m<sup>2</sup>/g, and 40.809 m<sup>2</sup>/g for CdS, CdS/Ag<sub>3</sub>PO<sub>4</sub>, and Pt-Ag<sub>3</sub>PO<sub>4</sub>/CdS/chitosan, respectively. The higher BET specific surface area of the CdS/Ag<sub>3</sub>PO<sub>4</sub> composite compared with pure CdS can be ascribed to the introduction of

$\text{Ag}_3\text{PO}_4$  particles in the composite and is beneficial to improve the catalytic performance. Furthermore, the nanocomposite of  $\text{Pt-Ag}_3\text{PO}_4/\text{CdS}/\text{chitosan}$  has a higher specific surface area compared with  $\text{CdS}/\text{Ag}_3\text{PO}_4$ , which is mainly due to the presence of chitosan. In fact, the matrix of chitosan effectively prevented the aggregation of the NPs, as highly dispersed NPs on chitosan matrix are obtained. Finally, the high specific surface area of the  $\text{Pt-Ag}_3\text{PO}_4/\text{CdS}/\text{chitosan}$  nanocomposite showed significant adsorption capacity of this sample, and it is one of the main reasons for its high photocatalytic activity. The Barrett, Joyner, Halenda (BJH) plot for  $\text{Pt-Ag}_3\text{PO}_4/\text{CdS}/\text{chitosan}$  nanocomposite, in Figure 4d, depicts that the mesopore size distribution estimated by the BJH method is around 1.85 nm.

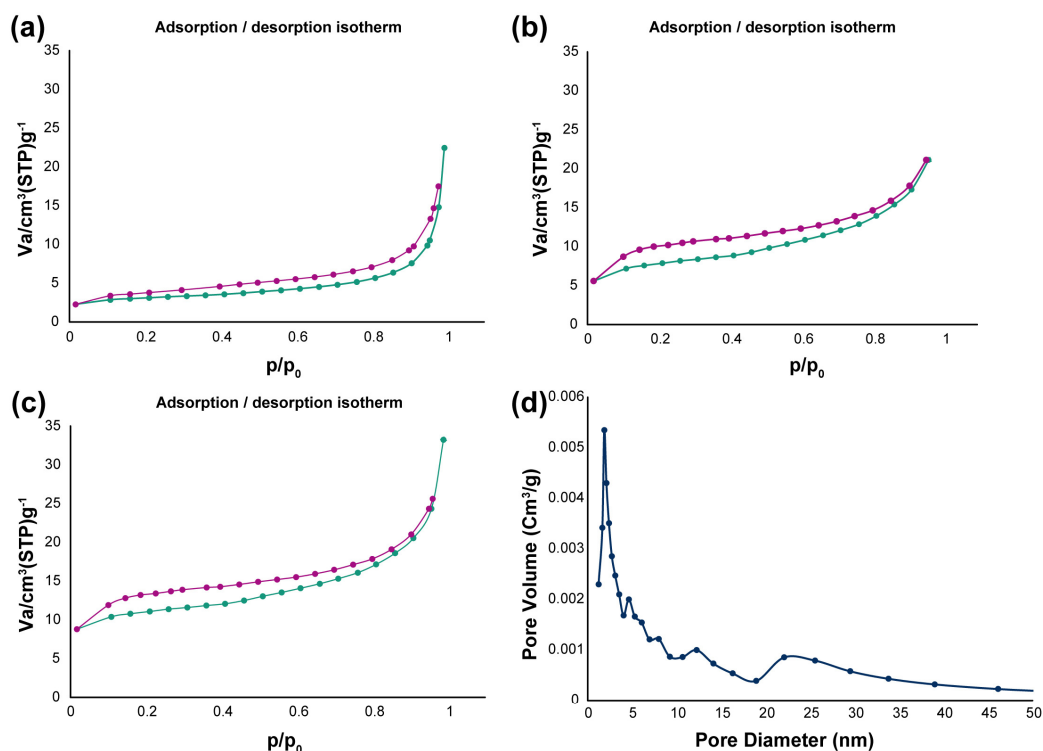


**Figure 4.** BET surface area of (a) CdS, (b) CdS/Ag<sub>3</sub>PO<sub>4</sub>, and (c) Pt-Ag<sub>3</sub>PO<sub>4</sub>/CdS/chitosan. (d) Pore size distribution plot (BJH plot) of Pt-Ag<sub>3</sub>PO<sub>4</sub>/CdS/chitosan.

FESEM micrograph was utilized to investigate the morphology of the CdS, Ag<sub>3</sub>PO<sub>4</sub>, chitosan, and Pt-Ag<sub>3</sub>PO<sub>4</sub>/CdS/chitosan samples. Spherical CdS NPs with several aggregations were observed in Figure 5a, whereas Figure 5b shows the morphology of the prepared Ag<sub>3</sub>PO<sub>4</sub> NPs, which have irregular particles. Figure 5c depicts that chitosan has a flaky nature with a relatively rough surface, which can be related to strong interactions between chitosan molecules. The FESEM image of Pt-Ag<sub>3</sub>PO<sub>4</sub>/CdS/chitosan in Figure 5d exhibits the presence of spherical CdS NPs as well as irregular particles of Ag<sub>3</sub>PO<sub>4</sub> in the nanocomposite of Pt-Ag<sub>3</sub>PO<sub>4</sub>/CdS/chitosan. The presence of NPs on the surface of chitosan as the matrix is clearly observed in Figure 5d. Energy dispersive X-ray (EDX) analysis (Figure 5e) confirms the composition of the NPs, which illustrated that Pt-Ag<sub>3</sub>PO<sub>4</sub>/CdS/chitosan comprises Pt, Cd, S, Ag, O, and C elements. All of these results are in good agreement with the transmission electron microscopy (TEM) images as shown in Figure 6 and the EDX table in Figure 5f. Based on the TEM images, the size of the nanocomposites is in the range of 80 to 150 nm, which is in good agreement with the FESEM images. In addition, some aggregations were observed compared with the CdS and Ag<sub>3</sub>PO<sub>4</sub> compartments, which are due to the presence of chitosan substrate as well as different NPs.

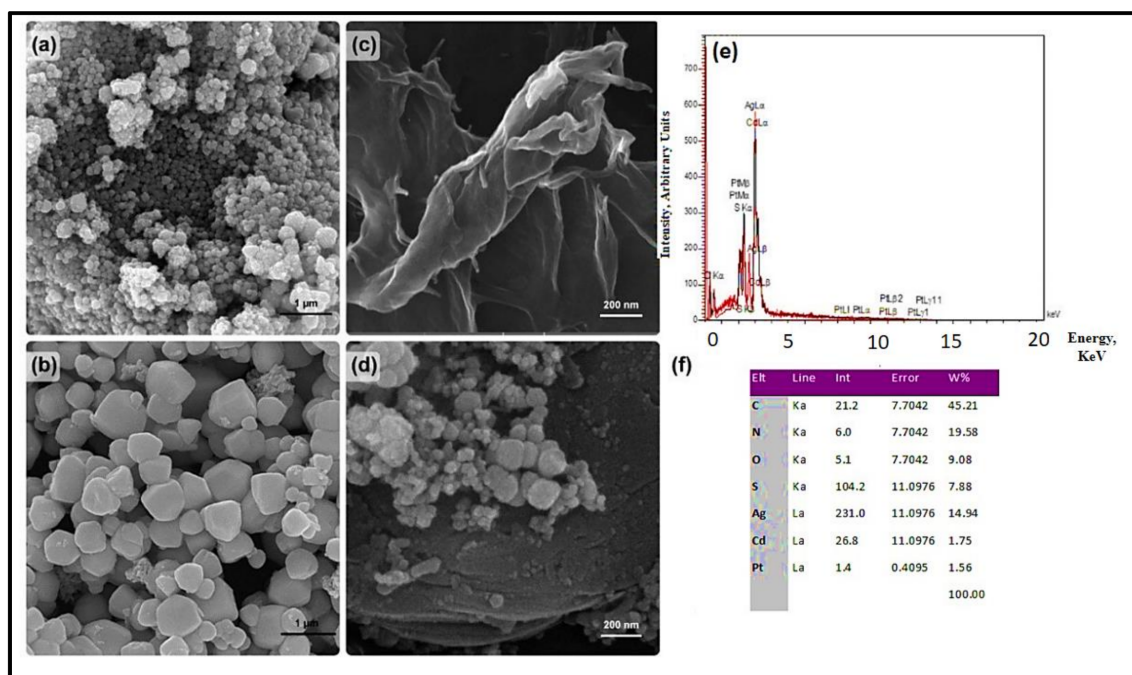


**Figure 5.** Field emission scanning electron microscope (FESEM) image of (a) CdS, (b)  $\text{Ag}_3\text{PO}_4$ , (c) chitosan, and (d) Pt- $\text{Ag}_3\text{PO}_4/\text{CdS}/\text{chitosan}$ . (e) EDS spectrum of Pt- $\text{Ag}_3\text{PO}_4/\text{CdS}/\text{chitosan}$ . (f) EDS table of Pt- $\text{Ag}_3\text{PO}_4/\text{CdS}/\text{chitosan}$ .

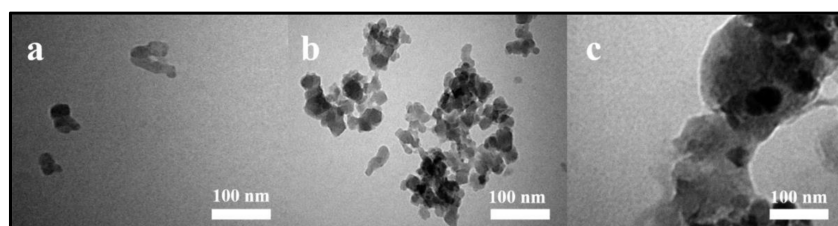


**Figure 6.** TEM image of (a) CdS, (b)  $\text{Ag}_3\text{PO}_4$ , and (c) Pt- $\text{Ag}_3\text{PO}_4/\text{CdS}/\text{chitosan}$ .

### 3.2. Photocatalytic Performance for MB Degradation

The maximum photodegradation rate of MB was obtained through the use of Pt- $\text{Ag}_3\text{PO}_4/\text{CdS}/\text{chitosan}$  catalyst. As shown in Figure 7a, MB was stable in the dark situation or under visible-light irradiation in the absence of any catalysts. NPs of CdS,  $\text{Ag}_3\text{PO}_4$ , and CdS/ $\text{Ag}_3\text{PO}_4$  adsorbed a little amount of MB under dark conditions. However, Pt- $\text{Ag}_3\text{PO}_4/\text{CdS}/\text{chitosan}$  composite showed perfect adsorption capacity (~37% in dark time) and the dye removal rate increased (~92% at 90 min) for MB. The experimental results revealed that the percentage of MB removal was found to be 53% and 81% in the presence of the CdS/ $\text{Ag}_3\text{PO}_4$  and CdS/ $\text{Ag}_3\text{PO}_4/\text{chitosan}$  photocatalyst, respectively.

The improved photocatalytic performance of the CdS/ $\text{Ag}_3\text{PO}_4$  sample compared with pure CdS or  $\text{Ag}_3\text{PO}_4$  sample is attributed to the presence of  $\text{Ag}_3\text{PO}_4$  NPs. The photogenerated electrons were transferred from the CdS CB into the  $\text{Ag}_3\text{PO}_4$  CB and the holes that had been photogenerated were transferred from the VB of  $\text{Ag}_3\text{PO}_4$  into the VB of CdS. This can reduce the recombination rate of  $e^-/h^+$  pairs.

Moreover, the introduction of chitosan as a good carrier into CdS/ $\text{Ag}_3\text{PO}_4$  nanocomposite increased the adsorption of dye, and this issue can be effective in improving the performance of the prepared nanocomposite.

In addition, because of the presence of chitosan matrix and Pt NPs in the CdS/ $\text{Ag}_3\text{PO}_4/\text{chitosan}$  nanocomposite, the catalytic performance of this photocatalyst significantly increased; Pt NPs can play an important role in the photodegradation process as they delay the recombination rate of  $e^-/h^+$  pairs. In fact, these NPs with large work functions are used as the electron sinks to trap the

photoinduced electrons from the CB of  $\text{Ag}_3\text{PO}_4$ , thus the lifetime of the photoinduced charge carriers can be prolonged.

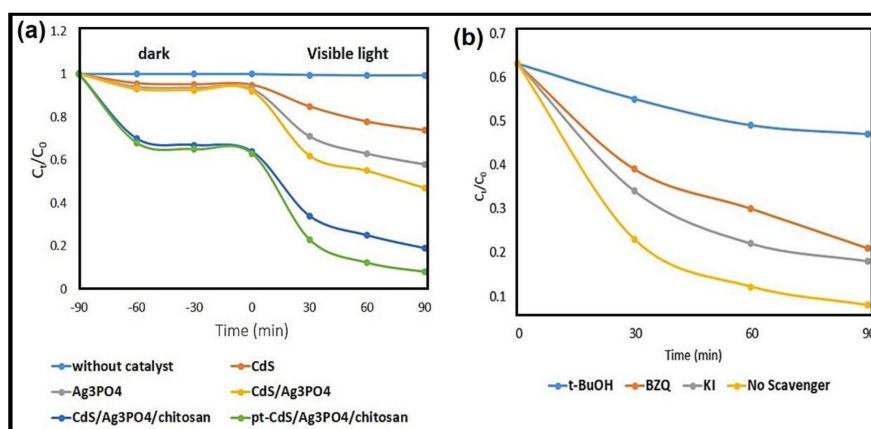


**Figure 7.** (a) The degradation efficiency for methylene blue (MB) ( $10^{-5}$  mol/L) removal in the process of prepared samples under visible light irradiation. (b) Effect of various scavengers on the degradation of MB by Pt- $\text{Ag}_3\text{PO}_4/\text{CdS}/\text{chitosan}$ .

### 3.3. Possible Photocatalytic Mechanism

In order to increase the photocatalytic activity of a catalyst, it is imperative to use various structures with matched bands of different semiconductors for the formation and the separation of photoinduced  $e^-/h^+$  pairs. The bandgap for CdS and  $\text{Ag}_3\text{PO}_4$  is 2.52 eV and 1.92 eV, respectively [32,43]. The CB potential of CdS is more negative than that CB of  $\text{Ag}_3\text{PO}_4$ . The photoinduced electrons on the CB of CdS migrate to the CB of  $\text{Ag}_3\text{PO}_4$  and the VB photogenerated holes of  $\text{Ag}_3\text{PO}_4$  could migrate to CdS. The CdS and  $\text{Ag}_3\text{PO}_4$  electron transfer was assessed by the energy of bandgap of Pt- $\text{Ag}_3\text{PO}_4/\text{CdS}/\text{chitosan}$  composite (1.6 eV). It should be noted that  $\text{Ag}_3\text{PO}_4$  and CdS NPs are intimately connected by the matrix of the chitosan in Pt- $\text{Ag}_3\text{PO}_4/\text{CdS}/\text{chitosan}$  composite.

The ability of adsorption and formation of  $e^-/h^+$  pairs have a direct relationship with the photocatalytic efficiency of the synthesized nanocomposite; Pt NPs play the role of a co-catalyst in the photodegradation process and delay the recombination rate of  $e^-/h^+$  pairs.

According to the BET results (Figure 4c), the Pt- $\text{Ag}_3\text{PO}_4/\text{CdS}/\text{chitosan}$  composite possessed a large specific surface area ( $40.809 \text{ m}^2/\text{g}$ ). In fact, Pt- $\text{Ag}_3\text{PO}_4/\text{CdS}$  photocatalyst onto the chitosan matrix effectively prevented the aggregation of the NPs and increased the specific surface area of the prepared catalyst.

The proposed photocatalytic reaction mechanism of Pt- $\text{Ag}_3\text{PO}_4/\text{CdS}/\text{chitosan}$  composite can be expressed as follows.

Initially, both CdS and  $\text{Ag}_3\text{PO}_4$  were excited simultaneously to form a pair of  $e^-/h^+$  driven by irradiation (visible light), after which the electrons that had been photogenerated were transferred from the CdS CB into the  $\text{Ag}_3\text{PO}_4$  CB, and then electrons transport from the  $\text{Ag}_3\text{PO}_4$  CB to the Pt NPs. In this step, the Pt NPs efficiently trap the photogenerated electrons because of their capacity in the reservoir of the  $e^-$ . On the other hand, the holes that had been photogenerated were transferred from the VB of  $\text{Ag}_3\text{PO}_4$  into the VB of CdS. Finally, the photogenerated electrons react with  $\text{O}_2$  to generate  $\text{O}_2^{\bullet-}$ , which then reacts with  $\text{H}^+$  to form  $\bullet\text{OOH}$ , with the quick decomposition to  $\bullet\text{OH}$ . Additionally, the holes oxidize  $\text{H}_2\text{O}$  and  $-\text{OH}$  to form  $\bullet\text{OH}$ , an important species in the process of photodegradation of organic pollutants. So, the process of  $\bullet\text{OH}$  radicals' formation can occur through two pathways, as shown in Figure 8. In conclusion, the prepared catalyst of Pt- $\text{Ag}_3\text{PO}_4/\text{CdS}/\text{chitosan}$  efficiently decreases the recombination rate of  $e^-/h^+$  charge carriers, thus enhancing the photocatalytic effectively and avoiding the photo corrosion of  $\text{Ag}_3\text{PO}_4$  ( $\text{Ag}^+ + e^- \rightarrow \text{Ag}$ ). Thus, the Pt- $\text{Ag}_3\text{PO}_4/\text{CdS}/\text{chitosan}$  catalyst is significantly stable and active in comparison with pure CdS or  $\text{Ag}_3\text{PO}_4$  [33].

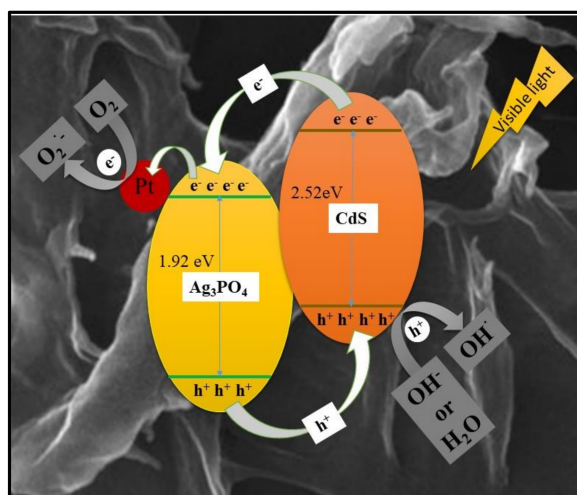


**Figure 8.** Proposed photocatalytic mechanism of Pt-Ag<sub>3</sub>PO<sub>4</sub>/CdS/chitosan under visible light.

### 3.4. Effect of Reactive Species on Photodegradation of MB

To investigate the possible photodegradation mechanism of MB by Pt-Ag<sub>3</sub>PO<sub>4</sub>/CdS/chitosan, various scavengers were added to the mixture in order to quench the relevant active species. In this study, *t*-BuOH, BZQ, and KI were chosen to be the scavengers of hydroxyl radicals ( $\bullet\text{OH}$ ), superoxide radicals ( $\text{O}_2^{\bullet-}$ ), and holes ( $\text{h}^+$ ), respectively. As depicted in Figure 7b, the photocatalytic degradation efficiency for MB with Pt-Ag<sub>3</sub>PO<sub>4</sub>/CdS/chitosan was about 92% after 90 min under visible light illumination, which was affected slightly in the presence of BZQ and KI, demonstrating that superoxide radicals and holes played a small role in the photodegradation of MB. However, the photocatalytic activity of the Pt-Ag<sub>3</sub>PO<sub>4</sub>/CdS/chitosan was completely suppressed by *t*-BuOH, indicating that  $\bullet\text{OH}$  plays the most important role in this photodegradation process; the percentage of MB removal was about 53%, 79%, and 82% in the presence of *t*-BuOH, BZQ, and KI scavengers, respectively. Consequently, the photodegradation of MB was lessened most remarkably in the presence of *t*-BuOH, suggesting that oxidation reaction was mediated mainly via hydroxyl radicals.

### 3.5. Recyclability of Pt-Ag<sub>3</sub>PO<sub>4</sub>/CdS/Chitosan Nanocomposites

Figure 9c shows the MB solution photodegradation in the four successive runs under the same condition. After each run, Pt-Ag<sub>3</sub>PO<sub>4</sub>/CdS/chitosan photocatalyst was washed with double distilled water several times, and a fresh solution of the dye was applied for the next run. The percentage of MB removal of Pt-Ag<sub>3</sub>PO<sub>4</sub>/CdS/chitosan photocatalyst was 92%, 90%, 87%, and 84% after 90 min of illumination time, respectively. It is important to note that the efficiency of photocatalytic activity of the synthesized nanocomposite had only a small reduction after four consecutive tests, indicating that the photocatalyst functioned as an effective catalyst with significant stability. Comparatively, the photodegradation of MB in the presence of pure CdS and Ag<sub>3</sub>PO<sub>4</sub> for the four types of recycling was about 26%, 19%, 11%, 7% and 42%, 22%, 13%, 10% after 90 min of visible light illumination, respectively (Figure 9a,b).

According to the acquired results, the NPs of CdS and Ag<sub>3</sub>PO<sub>4</sub> have poor stability against photocorrosion; low structural stability of pure Ag<sub>3</sub>PO<sub>4</sub> has been extensively explored earlier [79–83], where an excess of metallic Ag<sup>0</sup> species on the surface of Ag<sub>3</sub>PO<sub>4</sub>, resulting from the photocorrosion, sharply degraded the photochemical stabilities and shielded the light. Figure S4 illustrates the XRD patterns for Pt-Ag<sub>3</sub>PO<sub>4</sub>/CdS/chitosan nanocomposite before and after photodegradation process; a weak peak at  $2\theta \sim 38.3^\circ$  appeared after four cycling runs ascribable to the (111) crystalline plane of metallic Ag (JCPDS No. 65-2871), indicating that a little amount of Ag<sup>0</sup> species formed on the catalyst's surface. The ensuing Ag<sup>0</sup> species, which deposited on the surface of the catalyst, could scatter the photoinduced electrons, inhibited the further photoreduction of Ag<sup>+</sup> ions, thereby promoting

separation of charge carriers [33,83]. The immobilization of CdS and  $\text{Ag}_3\text{PO}_4$  NPs on the chitosan matrix could remarkably inhibit the dissolution of CdS and  $\text{Ag}_3\text{PO}_4$  during the photoreaction assay, thus contributing to the stability of aforementioned photocatalyst. Moreover, the presence of Pt NPs on the surface of catalysts could trap the photogenerated electrons as they improve the photocatalytic property of the Pt- $\text{Ag}_3\text{PO}_4/\text{CdS}/\text{chitosan}$  nanocomposite [84–90].

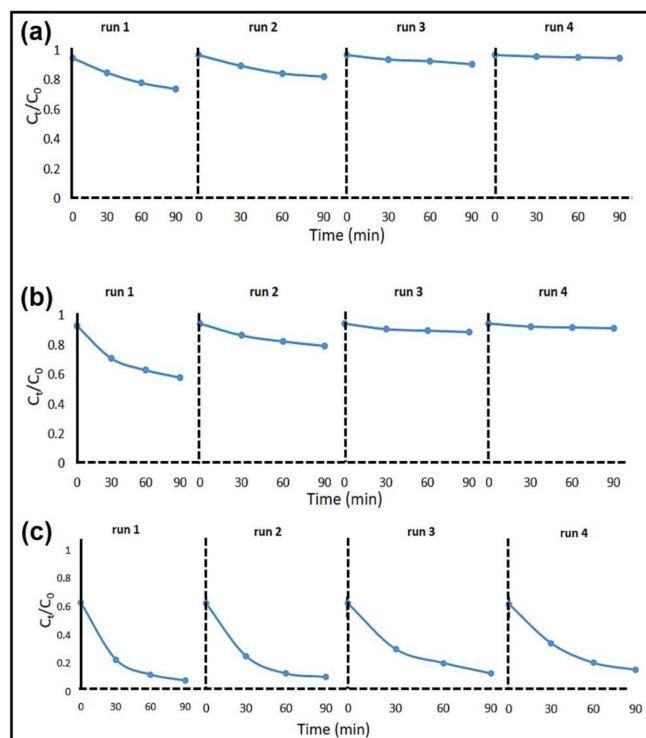


**Figure 9.** Recycling studies of (a) CdS, (b)  $\text{Ag}_3\text{PO}_4$ , and (c) Pt- $\text{Ag}_3\text{PO}_4/\text{CdS}/\text{chitosan}$  photocatalyst for the photodegradation of MB solution.

### 3.6. Antibacterial Tests

Cadmium sulfide (CdS) as another well-known narrow bandgap semiconductor has been confirmed to be capable of promoting the carrier transfer and increasing the light absorption [91] when combined with other materials such as  $\text{AgNO}_3$ . Thus, the nanocomposite preparation of  $\text{Ag}_3\text{PO}_4$  and CdS was expected to enhance photocatalytic activity [92]. In addition, decorating the prepared photocatalysts with noble metal NPs, such as Pt, is ideal way to increase the photocatalytic activity and photocatalytic antibacterial properties. So, Pt- $\text{Ag}_3\text{PO}_4/\text{CdS}/\text{chitosan}$  nanocomposite improves the utilization efficiency of light for antibacterial activity under visible light [93].

To investigate the antibacterial activity, the well disk-diffusion method was used to detect the standard antibiotics such as *Penicillin* and *Gentamicin* that have inhibitory action with outstanding zone of inhibition on the microorganisms and used for the examination of *Escherichia coli*, *Pseudomonas aeruginosa*, *Salmonella typhimurium*, *Staphylococcus aureus*, *Klebsiella pneumoniae*, and *Bacillus cereus* bacteria in a Tryptic soy agar medium. In this work, the antibacterial activity of Pt- $\text{Ag}_3\text{PO}_4/\text{CdS}/\text{chitosan}$  nanocomposite was investigated from 0 to 20  $\mu\text{g}/\text{mL}$  under visible light and in the dark; at a concentration of 20  $\mu\text{g}/\text{mL}$ , very good results were obtained. The antibacterial activity in the dark was much lower than in the light. The experiments were carried out in contrast with CdS, CdS- $\text{Ag}_3\text{PO}_4$ , standard antibiotic *Penicillin*, and *Gentamicin* using ( $\text{H}_2\text{O}$  as a negative control) by measuring zone of inhibition in mm and the experimental outcomes are shown in Figure 10. Antibacterial activity by Pt- $\text{Ag}_3\text{PO}_4/\text{CdS}/\text{chitosan}$  nanocomposite against six bacterial pathogens is due to the release of ROS (reactive oxygen species), which causes damage to the nucleic acids and membrane proteins [65,94,95].

Figure S5 depicts the antibacterial activity of the prepared samples at 20  $\mu\text{g}/\text{mL}$  under visible light tested by a well diffusion method on the model of different bacteria.

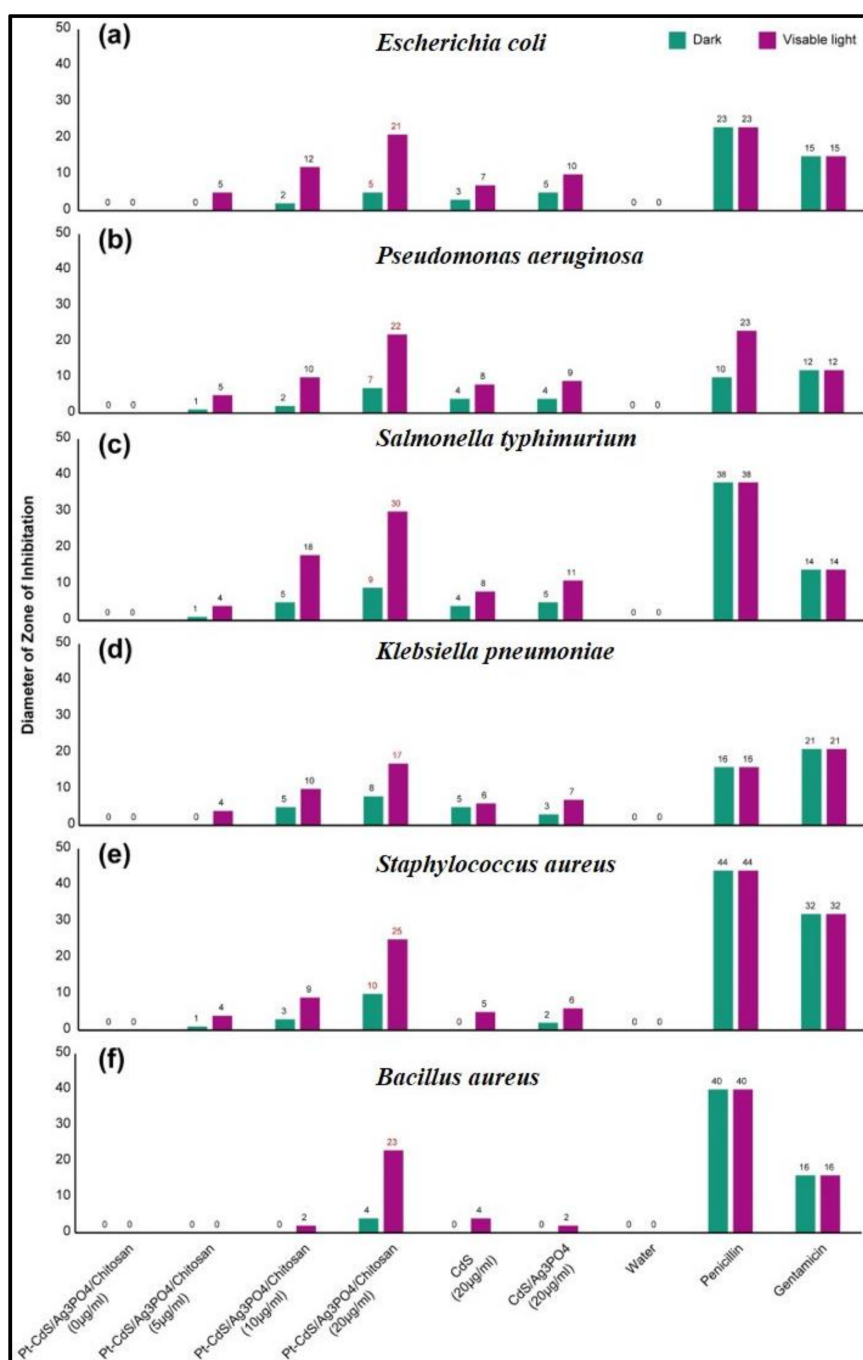


**Figure 10.** Antibacterial activity study of the prepared samples at different concentrations on the model (a) *Escherichia coli*, (b) *Pseudomonas aeruginosa*, (c) *Salmonella typhimurium*, (d) *Klebsiella pneumoniae*, (e) *Staphylococcus aureus*, and (f) *Bacillus cereus* bacterium under dark and visible light were tested by the well diffusion method based on diameter of zone of inhibition (mm). Water is negative control.

### 3.7. Cytotoxicity Assays

The cell viability in different cell lines was investigated after treatment (24- and 48-h time points) with the nanocomposite, and for each part of the nanosystem (Figure 11). The results clearly showed that the Ag<sub>3</sub>PO<sub>4</sub> part has cell viability of more than (61%, 56%, 60%, and 67%) in low concentrations and

(54%, 47%, 51%, and 56%) in the highest concentrations (results of HEK-293, HeLa, HepG2, and PC12 cell lines, respectively, after 24 h of treatment), and the cell viability of more than (57%, 69%, 55%, and 70%) in low concentrations and (50%, 45%, 26% and 68%) in the highest concentrations (results of HEK-293, HeLa, HepG2 and PC12 cell lines, respectively, after 48 h of treatment). By addition of this part,  $\text{Ag}_3\text{PO}_4$ , to the CdS/chitosan nanocomposite, the cell viability of the CdS/chitosan changes from (71%, 65%, 69%, and 67%) to (70%, 69%, 79%, and 59%) in low concentrations and from (62%, 51%, 54%, and 34%) to (61%, 53%, 61%, and 50%) in the highest concentrations (results of HEK-293, HeLa, HepG2 and PC12 cell lines, respectively, after 24 h of treatment). By addition of this part,  $\text{Ag}_3\text{PO}_4$ , to the CdS/chitosan nanocomposite, the cell viability of the CdS/chitosan changes from (66%, 62%, 67%, and 71%) to (65%, 67%, 69%, and 70%) in low concentrations and from (57%, 34%, 40%, and 34%) to (56%, 56%, 60%, and 50%) in the highest concentrations (results of HEK-293, HeLa, HepG2 and PC12 cell lines, respectively, after 48 h of treatment). Interestingly, the role of the addition of the  $\text{Ag}_3\text{PO}_4$  to the carbon-based substrate of CdS/chitosan showed gradual increases in the cell viability, and addition of the Pt to the nanocomposite leads to significant increase in the cell viability. Overall, the cell viability of the final nanocomposite, Pt- $\text{Ag}_3\text{PO}_4/\text{CdS}/\text{chitosan}$ , was recorded as more than 75% in low concentrations and 61% in high concentrations in both 24 and 48 h of treatment. Based on the available literature [96,97], CdS NPs can endorse the cytotoxic effect in different cell lines including HepG2, HeLa, PC12, and HEK-293 cell lines. However, in this study, the cytotoxicity effect promoted by addition of CdS was much lower, which may be because of the unavailable CdS sites on the surface. Additionally,  $\text{Ag}_3\text{PO}_4$  could also considerably elevate cytotoxicity in the mentioned cell lines [98,99]. In this study, however, some cytotoxicity was discerned because of  $\text{Ag}_3\text{PO}_4$ , but it was not in the significant range documented in the literature.

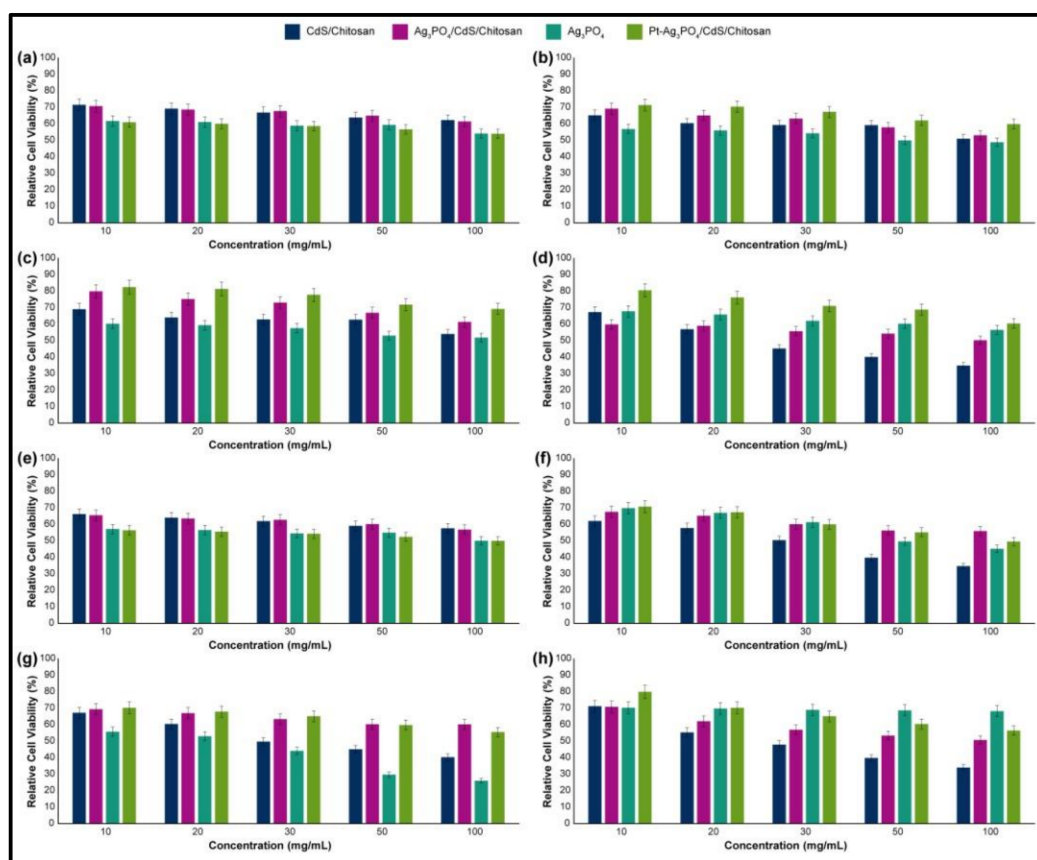


**Figure 11.** MTT results of the CdS/Chitosan,  $\text{Ag}_3\text{PO}_4/\text{CdS}/\text{chitosan}$ ,  $\text{Ag}_3\text{PO}_4$ , and Pt- $\text{Ag}_3\text{PO}_4/\text{CdS}/\text{chitosan}$  on (a) HEK-293, (b) HeLa, (c) HepG2, and (d) PC12 cell lines after 24 h of treatment; and on (e) HEK-293, (f) HeLa, (g) HepG2, and (h) PC12 after 48 h of treatment.

#### 4. Conclusions

In summary, the present study describes a facile and inexpensive method to prepare Pt-Ag<sub>3</sub>PO<sub>4</sub>/CdS/chitosan nanocomposite, wherein the synergistic effect among Pt, CdS, Ag<sub>3</sub>PO<sub>4</sub>, and chitosan could increase the response of the composite to visible light-induced photocatalysis and antibacterial activities. These outstanding performances can be related to several factors. Coupling of CdS and Ag<sub>3</sub>PO<sub>4</sub> could promote the separation of charge carriers. Consequently, the CdS/Ag<sub>3</sub>PO<sub>4</sub> composite does not suffer from photo corrosion during the photodegradation process. Furthermore, the immobilization of CdS and Ag<sub>3</sub>PO<sub>4</sub> NPs on the matrix of chitosan could significantly inhibit CdS and Ag<sub>3</sub>PO<sub>4</sub> from dissolution during the photoreaction, thus promoting the stability of the photocatalyst. Moreover, chitosan can play a significant role in the adsorption of organic pollutants and it is helpful in improving the efficiency of the prepared nanocomposite.

The presence of Pt NPs on the surface of the prepared composite can delay the recombination rate of e<sup>-</sup>/h<sup>+</sup> pairs. These NPs with large work functions have been used as the electron sinks to trap the photoinduced electrons from the CB of Ag<sub>3</sub>PO<sub>4</sub>, thus prolonging the lifetime of the photoinduced charge carriers. Consequently, the prepared Pt-Ag<sub>3</sub>PO<sub>4</sub>/CdS/chitosan nanocomposite effectively depressed the recombination of e<sup>-</sup>/h<sup>+</sup> charge carriers and improved the photocatalytic activity, while avoiding the photocorrosion of Ag<sub>3</sub>PO<sub>4</sub> (Ag<sup>+</sup> + e<sup>-</sup> → Ag). The antibacterial experiments exhibit that the Pt-Ag<sub>3</sub>PO<sub>4</sub>/CdS/chitosan nanocomposite is endowed with considerable antibacterial activity against six types of gram-positive and gram-negative bacteria in a short time under exposure to the visible light, a significant advantage being the low consumption of nanocomposite for attaining the antibacterial activity. The loading of Pt NPs can enhance the antibacterial activity of nanocomposite in the dark and under the visible light. Hence, this work describes an ideal approach to prepare a new and useful nanocomposite of Pt-Ag<sub>3</sub>PO<sub>4</sub>/CdS/chitosan for multiple appliances and may stimulate further innovative combinations.

**Supplementary Materials:** The following are available online at <http://www.mdpi.com/2079-4991/10/11/2320/s1>, Figure S1: The emission wavelength of the light source of NVSWE21AT; Figure S2: FT-IR spectrum of Ag<sub>3</sub>PO<sub>4</sub>; Figure S3: XRD patterns of Ag<sub>3</sub>PO<sub>4</sub>; Figure S4: XRD pattern of Ag<sub>3</sub>PO<sub>4</sub>/CS/CdS nanocomposites before and after four cycling runs; Figure S5: Antibacterial activity picture of the prepared samples at 20 µg/mL under visible light were tested by the well diffusion method on the model of different bacterium (a) *E. coli*, (b) *Pseudomonas aeruginosa*, (c) *Salmonella typhimurium*, (d) *Klebsiella pneumonia*, (e) *Staphylococcus aureus*, and (f) *Bacillus cereus*.

**Author Contributions:** Conceptualization, M.K., M.B., R.K., and N.R.; Methodology, M.K., M.B., R.K., Y.F., and N.R.; Validation, M.K., M.B., R.K., and R.D.; Formal Analysis, M.K., Y.F., R.K., and M.S.; Investigation, M.K., M.B., R.K., H.W.J., and N.R.; Resources, M.B., R.D., R.S.V., M.S., and H.W.J.; Writing—Original Draft Preparation, M.K., M.B., R.K., and N.R.; Writing—Review & Editing, M.K., H.W.J., R.K., M.S., R.S.V., and N.R.; Visualization, Y.F. and M.S.; Supervision, M.B., M.S., and R.S.V.; Project administration, M.B.; Funding acquisition, M.B. and M.S. All authors have read and agreed to the published version of the manuscript.

**Funding:** This research was funded by Sharif University of Technology Research Council and the National Science Foundation of Korea.

**Acknowledgments:** M.B. acknowledges the Research Council of Sharif University of Technology for the research funding of this project. This research was supported by National Research Foundation of Korea (NRF) funded by the Ministry of Science and ICT (2020M2D8A206983011). Furthermore, the financial support of the Basic Science Research Program (2017R1A2B3009135) through the National Research Foundation of Korea is appreciated.

**Conflicts of Interest:** The authors declare no conflict of interest.

#### References

1. Zakerzadeh, E.; Alizadeh, E.; Samadi Kafil, H.; Mohammad Hassanzadeh, A.; Salehi, R.; Mahkam, M. Novel antibacterial polymeric nanocomposite for smart co-delivery of anticancer drugs. *Artif. Cells Nanomed. Biotechnol.* **2017**, *45*, 1509–1520. [[CrossRef](#)] [[PubMed](#)]
2. Jiang, H.; Zhang, G.; Xu, B.; Feng, X.; Bai, Q.; Yang, G.; Li, H. Thermosensitive antibacterial Ag nanocomposite hydrogels made by a one-step green synthesis strategy. *New J. Chem.* **2016**, *40*, 6650–6657. [[CrossRef](#)]
3. Yadollahi, M.; Farhoudian, S.; Namazi, H. One-pot synthesis of antibacterial chitosan/silver bio-nanocomposite hydrogel beads as drug delivery systems. *Int. J. Biol. Macromol.* **2015**, *79*, 37–43. [[CrossRef](#)] [[PubMed](#)]

4. Sood, S.; Kumar, A.; Sharma, N. Photocatalytic and antibacterial activity studies of ZnO nanoparticles synthesized by thermal decomposition of mechanochemically processed oxalate precursor. *Chem. Sel.* **2016**, *1*, 6925–6932. [[CrossRef](#)]
5. Amornpitoksuk, P.; Suwanboon, S.; Sangkanu, S.; Sukhoom, A.; Wudtipan, J.; Srijan, K.; Kaewtaro, S. Synthesis, photocatalytic and antibacterial activities of ZnO particles modified by diblock copolymer. *Powder Technol.* **2011**, *212*, 432–438. [[CrossRef](#)]
6. Safdar, M.; Ozaslan, M.; Khailany, R.A.; Latif, S.; Junejo, Y.; Saeed, M.; Al-Attar, M.S.; Kanabe, B.O. Synthesis, Characterization and Applications of a Novel Platinum-Based Nanoparticles: Catalytic, Antibacterial and Cytotoxic Studies. *J. Inorg. Organomet. Polym. Mater.* **2020**, *30*, 2430–2439. [[CrossRef](#)]
7. David, L.; Moldovan, B. Green Synthesis of Biogenic Silver Nanoparticles for Efficient Catalytic Removal of Harmful Organic Dyes. *Nanomaterials* **2020**, *10*, 202. [[CrossRef](#)]
8. Liu, X.; Qi, S.; Li, Y.; Yang, L.; Cao, B.; Tang, C.Y. Synthesis and characterization of novel antibacterial silver nanocomposite nanofiltration and forward osmosis membranes based on layer-by-layer assembly. *Water Res.* **2013**, *47*, 3081–3092. [[CrossRef](#)]
9. Mahiuddin, M.; Saha, P.; Ochiai, B. Green Synthesis and Catalytic Activity of Silver Nanoparticles Based on Piper chaba Stem Extracts. *Nanomaterials* **2020**, *10*, 1777. [[CrossRef](#)]
10. Kourtis, A.P.; Hatfield, K.; Baggs, J.; Mu, Y.; See, I.; Epson, E.; Nadle, J.; Kainer, M.A.; Dumyati, G.; Petit, S. Vital Signs: Epidemiology and Recent Trends in Methicillin-Resistant and in Methicillin-Susceptible *Staphylococcus aureus* Bloodstream Infections—United States. *Morb. Mortal. Wkly. Rep.* **2019**, *68*, 214. [[CrossRef](#)]
11. SonDI, I.; Salopek-SonDI, B. Silver nanoparticles as antimicrobial agent: A case study on *E. coli* as a model for Gram-negative bacteria. *J. Colloid Interface Sci.* **2004**, *275*, 177–182. [[CrossRef](#)] [[PubMed](#)]
12. Mandal, S.K.; Brahmachari, S.; Das, P.K. In Situ Synthesised Silver Nanoparticle-Infused l-Lysine-Based Injectable Hydrogel: Development of a Biocompatible, Antibacterial, Soft Nanocomposite. *ChemPlusChem* **2014**, *79*, 1733–1746.
13. Turner, N.A.; Sharma-Kuinkel, B.K.; Maskarinec, S.A.; Eichenberger, E.M.; Shah, P.P.; Carugati, M.; Holland, T.L.; Fowler, V.G. Methicillin-resistant *Staphylococcus aureus*: An overview of basic and clinical research. *Nat. Rev. Microbiol.* **2019**, *17*, 203–218. [[CrossRef](#)] [[PubMed](#)]
14. Ogugbue, C.J.; Sawidis, T. Bioremediation and detoxification of synthetic wastewater containing triarylmethane dyes by *Aeromonas hydrophila* isolated from industrial effluent. *Biotechnol. Res. Int.* **2011**, *2011*. [[CrossRef](#)] [[PubMed](#)]
15. de Campos Ventura-Camargo, B.; Marin-Morales, M.A. Azo dyes: Characterization and toxicity—a review. *Text. Light Ind. Sci. Technol.* **2013**, *2*, 85–103.
16. Saif, S.; Tahir, A.; Chen, Y. Green synthesis of iron nanoparticles and their environmental applications and implications. *Nanomaterials* **2016**, *6*, 209. [[CrossRef](#)]
17. Lu, H.; Zhang, L.; Ma, J.; Alam, N.; Zhou, X.; Ni, Y. Nano-cellulose/MOF derived carbon doped CuO/Fe<sub>3</sub>O<sub>4</sub> nanocomposite as high efficient catalyst for organic pollutant remedy. *Nanomaterials* **2019**, *9*, 277. [[CrossRef](#)]
18. Fang, Y.; Wu, Q.; Li, H.; Zhang, B.; Yan, R.; Chen, J.; Sun, M. Photocatalytic activity of silver oxide capped Ag nanoparticles constructed by air plasma irradiation. *Appl. Phys. Lett.* **2018**, *112*, 163101. [[CrossRef](#)]
19. Ouyang, W.; Kuna, E.; Yopez, A.; Balu, A.M.; Romero, A.A.; Colmenares, J.C.; Luque, R. Mechanochemical synthesis of TiO<sub>2</sub> nanocomposites as photocatalysts for benzyl alcohol photo-oxidation. *Nanomaterials* **2016**, *6*, 93. [[CrossRef](#)] [[PubMed](#)]
20. Dasineh Khiavi, N.; Katal, R.; Kholghi Eshkalak, S.; Masudy-Panah, S.; Ramakrishna, S.; Jiangyong, H. Visible light driven heterojunction photocatalyst of CuO–Cu<sub>2</sub>O thin films for photocatalytic degradation of organic pollutants. *Nanomaterials* **2019**, *9*, 1011. [[CrossRef](#)] [[PubMed](#)]
21. Mills, A.; Le Hunte, S. An overview of semiconductor photocatalysis. *J. Photochem. Photobiol. A Chem.* **1997**, *108*, 1–35. [[CrossRef](#)]
22. Tryk, D.; Fujishima, A.; Honda, K. Recent topics in photoelectrochemistry: Achievements and future prospects. *Electrochim. Acta* **2000**, *45*, 2363–2376. [[CrossRef](#)]
23. Malato, S.; Fernández-Ibáñez, P.; Maldonado, M.I.; Blanco, J.; Gernjak, W. Decontamination and disinfection of water by solar photocatalysis: Recent overview and trends. *Catal. Today* **2009**, *147*, 1–59. [[CrossRef](#)]
24. Krishnamoorthy, K.; Mohan, R.; Kim, S.-J. Graphene oxide as a photocatalytic material. *Appl. Phys. Lett.* **2011**, *98*, 244101. [[CrossRef](#)]

25. Byrne, J.A.; Dunlop, P.S.M.; Hamilton, J.W.J.; Fernández-Ibáñez, P.; Polo-López, I.; Sharma, P.K.; Vennard, A.S.M. A review of heterogeneous photocatalysis for water and surface disinfection. *Molecules* **2015**, *20*, 5574–5615. [[CrossRef](#)]
26. Gatto, F.; Moglianetti, M.; Pompa, P.P.; Bardi, G. Platinum nanoparticles decrease reactive oxygen species and modulate gene expression without alteration of immune responses in THP-1 monocytes. *Nanomaterials* **2018**, *8*, 392. [[CrossRef](#)]
27. Baeg, E.; Sooklert, K.; Sereemasun, A. Copper oxide nanoparticles cause a dose-dependent toxicity via inducing reactive oxygen species in drosophila. *Nanomaterials* **2018**, *8*, 824. [[CrossRef](#)]
28. Yi, Z.; Ye, J.; Kikugawa, N.; Kako, T.; Ouyang, S.; Stuart-Williams, H.; Yang, H.; Cao, J.; Luo, W.; Li, Z. An orthophosphate semiconductor with photooxidation properties under visible-light irradiation. *Nat. Mater.* **2010**, *9*, 559–564. [[CrossRef](#)]
29. McEvoy, J.G.; Zhang, Z. Antimicrobial and photocatalytic disinfection mechanisms in silver-modified photocatalysts under dark and light conditions. *J. Photochem. Photobiol. C Photochem. Rev.* **2014**, *19*, 62–75. [[CrossRef](#)]
30. Amornpitoksuk, P.; Suwanboon, S.; Sangkanu, S.; Sukhoom, A.; Muensit, N.; Baltrusaitis, J. Synthesis, characterization, photocatalytic and antibacterial activities of Ag-doped ZnO powders modified with a diblock copolymer. *Powder Technol.* **2012**, *219*, 158–164. [[CrossRef](#)]
31. Xu, Y.-S.; Zhang, W.-D. Monodispersed Ag<sub>3</sub>PO<sub>4</sub> nanocrystals loaded on the surface of spherical Bi<sub>2</sub>MoO<sub>6</sub> with enhanced photocatalytic performance. *Dalton Trans.* **2013**, *42*, 1094–1101. [[CrossRef](#)] [[PubMed](#)]
32. Bagherzadeh, M.; Kaveh, R. New Magnetically Recyclable Reduced Graphene Oxide rGO/MFe<sub>2</sub>O<sub>4</sub> (M= Ca, Mg)/Ag<sub>3</sub>PO<sub>4</sub> Nanocomposites with Remarkably Enhanced Visible-light Photocatalytic Activity and Stability. *Photochem. Photobiol.* **2018**, *94*, 1210–1224. [[CrossRef](#)]
33. Cao, Q.; Xiao, L.; Zeng, L.; Cao, C.; Wang, J. Ag<sub>3</sub>PO<sub>4</sub>/chitosan/CdS nanocomposites exhibiting high photocatalytic activities under visible-light illumination. *Powder Technol.* **2017**, *321*, 1–8. [[CrossRef](#)]
34. Yao, W.; Zhang, B.; Huang, C.; Ma, C.; Song, X.; Xu, Q. Synthesis and characterization of high efficiency and stable Ag<sub>3</sub>PO<sub>4</sub>/TiO<sub>2</sub> visible light photocatalyst for the degradation of methylene blue and rhodamine B solutions. *J. Mater. Chem.* **2012**, *22*, 4050–4055. [[CrossRef](#)]
35. Zhao, F.-M.; Pan, L.; Wang, S.; Deng, Q.; Zou, J.-J.; Wang, L.; Zhang, X. Ag<sub>3</sub>PO<sub>4</sub>/TiO<sub>2</sub> composite for efficient photodegradation of organic pollutants under visible light. *Appl. Surf. Sci.* **2014**, *317*, 833–838. [[CrossRef](#)]
36. Li, Y.; Yu, L.; Li, N.; Yan, W.; Li, X. Heterostructures of Ag<sub>3</sub>PO<sub>4</sub>/TiO<sub>2</sub> mesoporous spheres with highly efficient visible light photocatalytic activity. *J. Colloid Interface Sci.* **2015**, *450*, 246–253. [[CrossRef](#)]
37. Samal, A.; Baral, A.; Das, D.P. Silver Phosphate Based Photocatalysis: A Brief Review from Fundamentals to Applications. *Photocatalytic Nanomater. Environ. Appl.* **2018**, *27*, 276–315.
38. Miyasato, R.; Fujiwara, M.; Sato, H.; Yano, T.; Hashimoto, H. Particle size effects of tetrahedron-shaped Ag<sub>3</sub>PO<sub>4</sub> photocatalyst on water-oxidation activity and carrier recombination dynamics. *Chem. Phys. Lett. X* **2019**, *2*, 100023. [[CrossRef](#)]
39. Guo, J.; Ouyang, S.; Zhou, H.; Kako, T.; Ye, J. Ag<sub>3</sub>PO<sub>4</sub>/In(OH)<sub>3</sub> composite photocatalysts with adjustable surface-electric property for efficient photodegradation of organic dyes under simulated solar-light irradiation. *J. Phys. Chem. C* **2013**, *117*, 17716–17724. [[CrossRef](#)]
40. Tang, J.; Gong, W.; Cai, T.; Xie, T.; Deng, C.; Peng, Z.; Deng, Q. Novel visible light responsive Ag@(Ag<sub>2</sub>S/Ag<sub>3</sub>PO<sub>4</sub>) photocatalysts: Synergistic effect between Ag and Ag<sub>2</sub>S for their enhanced photocatalytic activity. *RSC Adv.* **2013**, *3*, 2543–2547. [[CrossRef](#)]
41. Taddesse, D.; Anjejo, G.; Kebede, D. Zeolite Supported CdS/ZnO/Ag<sub>3</sub>PO<sub>4</sub> Nano-Composite: Synthesis, Characterization and Photocatalytic Activity for the Degradation of Methylene Blue. Ph.D. Thesis, Haramaya University, Haramaya, Ethiopia, 2017.
42. Berr, M.; Vaneski, A.; Susha, A.S.; Rodríguez-Fernández, J.; Döblinger, M.; Jäckel, F.; Rogach, A.L.; Feldmann, J. Colloidal CdS nanorods decorated with subnanometer sized Pt clusters for photocatalytic hydrogen generation. *Appl. Phys. Lett.* **2010**, *97*, 093108. [[CrossRef](#)]
43. Bagherzadeh, M.; Kaveh, R.; Ozkar, S.; Akbayrak, S. Preparation and characterization of a new CdS-NiFe<sub>2</sub>O<sub>4</sub>/reduced graphene oxide photocatalyst and its use for degradation of methylene blue under visible light irradiation. *Res. Chem. Intermed.* **2018**, *44*, 5953–5979. [[CrossRef](#)]
44. Lin, R.; Ding, Y. A review on the synthesis and applications of mesostructured transition metal phosphates. *Materials* **2013**, *6*, 217–243. [[CrossRef](#)] [[PubMed](#)]

45. Liu, J.; Fu, X.; Chen, S.; Zhu, Y. Electronic structure and optical properties of  $\text{Ag}_3\text{PO}_4$  photocatalyst calculated by hybrid density functional method. *Appl. Phys. Lett.* **2011**, *99*, 191903. [[CrossRef](#)]
46. Zhu, G.; Cheng, Z.; Lv, T.; Pan, L.; Zhao, Q.; Sun, Z. Zn-doped nanocrystalline  $\text{TiO}_2$  films for CdS quantum dot sensitized solar cells. *Nanoscale* **2010**, *2*, 1229–1232. [[CrossRef](#)]
47. Zhai, T.; Fang, X.; Li, L.; Bando, Y.; Golberg, D. One-dimensional CdS nanostructures: Synthesis, properties, and applications. *Nanoscale* **2010**, *2*, 168–187. [[CrossRef](#)]
48. Yu, J.; Yang, B.; Cheng, B. Noble-metal-free carbon nanotube- $\text{Cd}_{0.1}\text{Zn}_{0.9}\text{S}$  composites for high visible-light photocatalytic  $\text{H}_2$ -production performance. *Nanoscale* **2012**, *4*, 2670–2677. [[CrossRef](#)]
49. Cao, J.; Sun, J.Z.; Hong, J.; Li, H.Y.; Chen, H.Z.; Wang, M. Carbon Nanotube/CdS Core–Shell Nanowires Prepared by a Simple Room-Temperature Chemical Reduction Method. *Adv. Mater.* **2004**, *16*, 84–87. [[CrossRef](#)]
50. Bahnemann, D.; Kholuiskaya, S.; Dillert, R.; Kulak, A.; Kokorin, A. Photodestruction of dichloroacetic acid catalyzed by nano-sized  $\text{TiO}_2$  particles. *Appl. Catal. B Environ.* **2002**, *36*, 161–169. [[CrossRef](#)]
51. Jo, Y.K.; Kim, I.Y.; Lee, J.M.; Nahm, S.; Choi, J.-W.; Hwang, S.-J. Surface-anchored  $\text{CdS}@ \text{Ag}_3\text{PO}_4$  nanocomposite with efficient visible light photocatalytic activity. *Mater. Lett.* **2014**, *114*, 152–155. [[CrossRef](#)]
52. Chava, R.K.; Do, J.Y.; Kang, M. Fabrication of  $\text{CdS}-\text{Ag}_3\text{PO}_4$  heteronanostructures for improved visible photocatalytic hydrogen evolution. *J. Alloy. Compd.* **2017**, *727*, 86–93. [[CrossRef](#)]
53. Mirsalari, S.A.; Nezamzadeh-Ejhi, A.  $\text{CdS}-\text{Ag}_3\text{PO}_4$  nano-catalyst: A brief characterization and kinetic study towards methylene blue photodegradation. *Mater. Sci. Semicond. Process.* **2021**, *122*, 105455. [[CrossRef](#)]
54. Jing, Z.; Wang, C.; Wang, G.; Li, W.; Lu, D. Preparation and antibacterial activities of undoped and palladium doped titania nanoparticles. *J. Sol Gel Sci. Technol.* **2010**, *56*, 121–127. [[CrossRef](#)]
55. Lin, J.; Qu, W.; Zhang, S. Disposable biosensor based on enzyme immobilized on Au–chitosan-modified indium tin oxide electrode with flow injection amperometric analysis. *Anal. Biochem.* **2007**, *360*, 288–293. [[CrossRef](#)] [[PubMed](#)]
56. Li, J.; Cai, C.; Li, J.; Li, J.; Sun, T.; Wang, L.; Wu, H.; Yu, G. Chitosan-based nanomaterials for drug delivery. *Molecules* **2018**, *23*, 2661. [[CrossRef](#)]
57. Bandara, S.; Du, H.; Carson, L.; Bradford, D.; Kommalapati, R. Agricultural and Biomedical Applications of Chitosan-Based Nanomaterials. *Nanomaterials* **2020**, *10*, 1903. [[CrossRef](#)]
58. Kaczmarek, M.B.; Struszczyk-Swita, K.; Li, X.; Szczesna-Antczak, M.; Daroch, M. Enzymatic Modifications of Chitin, Chitosan and Chitooligosaccharides. *Front. Bioeng. Biotechnol.* **2019**, *7*, 243. [[CrossRef](#)]
59. Zhu, H.; Jiang, R.; Xiao, L.; Chang, Y.; Guan, Y.; Li, X.; Zeng, G. Photocatalytic decolorization and degradation of Congo Red on innovative crosslinked chitosan/nano-CdS composite catalyst under visible light irradiation. *J. Hazard. Mater.* **2009**, *169*, 933–940. [[CrossRef](#)]
60. Liu, S.; Guo, Z.; Qian, X.; Zhang, J.; Liu, J.; Lin, J. Sonochemical deposition of ultrafine metallic Pt nanoparticles on CdS for efficient photocatalytic hydrogen evolution. *Sustain. Energy Fuels* **2019**, *3*, 1048–1054. [[CrossRef](#)]
61. Zhao, X.; Guan, J.; Li, J.; Li, X.; Wang, H.; Huo, P.; Yan, Y.  $\text{CeO}_2/3\text{D g-C}_3\text{N}_4$  heterojunction deposited with Pt cocatalyst for enhanced photocatalytic  $\text{CO}_2$  reduction. *Appl. Surf. Sci.* **2021**, *537*, 147891. [[CrossRef](#)]
62. Wang, D.; Song, Y.; Cai, J.; Wu, L.; Li, Z. Effective photo-reduction to deposit Pt nanoparticles on MIL-100 (Fe) for visible-light-induced hydrogen evolution. *New J. Chem.* **2016**, *40*, 9170–9175. [[CrossRef](#)]
63. Boomi, P.; Prabhu, H.G.; Mathiyarasu, J. Synthesis, characterization and antibacterial activity of polyaniline/Pt–Pd nanocomposite. *Eur. J. Med. Chem.* **2014**, *72*, 18–25. [[CrossRef](#)] [[PubMed](#)]
64. Rahimi, N.; Doroodmand, M.M.; Ghahremani, A. Fabrication of a novel casein phosphopeptides/multi-walled carbon nanotubes/micro hybrid resin as mixed matrix membrane-junction reference electrode. *J. Electroanal. Chem.* **2015**, *745*, 98–105. [[CrossRef](#)]
65. Bharathi, D.; Vasantharaj, S.; Bhuvaneshwari, V. Green synthesis of silver nanoparticles using Cordia dichotoma fruit extract and its enhanced antibacterial, anti-biofilm and photo catalytic activity. *Mater. Res. Express* **2018**, *5*, 055404. [[CrossRef](#)]
66. Mutalik, C.; Wang, D.-Y.; Krisnawati, D.I.; Jazidie, A.; Yougbare, S.; Kuo, T.-R. Light-activated heterostructured nanomaterials for antibacterial applications. *Nanomaterials* **2020**, *10*, 643. [[CrossRef](#)]
67. Zhao, C.; Feng, B.; Li, Y.; Tan, J.; Lu, X.; Weng, J. Preparation and antibacterial activity of titanium nanotubes loaded with Ag nanoparticles in the dark and under the UV light. *Appl. Surf. Sci.* **2013**, *280*, 8–14. [[CrossRef](#)]
68. Plachá, D.; Muñoz-Bonilla, A.; Škrlová, K.; Echeverria, C.; Chiloeches, A.; Petr, M.; Lafdi, K.; Fernández-García, M. Antibacterial Character of Cationic Polymers Attached to Carbon-Based Nanomaterials. *Nanomaterials* **2020**, *10*, 1218. [[CrossRef](#)]

69. Fu, J.; Chang, B.; Tian, Y.; Xi, F.; Dong, X. Novel  $C_3N_4$ -CdS composite photocatalysts with organic-inorganic heterojunctions: In situ synthesis, exceptional activity, high stability and photocatalytic mechanism. *J. Mater. Chem. A* **2013**, *1*, 3083–3090. [[CrossRef](#)]
70. Guibal, E.; Cambe, S.; Bayle, S.; Taulemesse, J.-M.; Vincent, T. Silver/chitosan/cellulose fibers foam composites: From synthesis to antibacterial properties. *J. Colloid Interface Sci.* **2013**, *393*, 411–420. [[CrossRef](#)]
71. Botelho, G.; Andres, J.; Gracia, L.; Matos, L.S.; Longo, E. Photoluminescence and photocatalytic properties of  $Ag_3PO_4$  microcrystals: An experimental and theoretical investigation. *ChemPlusChem* **2016**, *81*, 202–212. [[CrossRef](#)]
72. Zhang, W.; Hu, C.; Zhai, W.; Wang, Z.; Sun, Y.; Chi, F.; Ran, S.; Liu, X.; Lv, Y. Novel  $Ag_3PO_4/CeO_2$  pn hierarchical heterojunction with enhanced photocatalytic performance. *Mater. Res.* **2016**, *19*, 673–679. [[CrossRef](#)]
73. Sepahvand, S.; Farhadi, S. Fullerene-modified magnetic silver phosphate ( $Ag_3PO_4/Fe_3O_4/C_{60}$ ) nanocomposites: Hydrothermal synthesis, characterization and study of photocatalytic, catalytic and antibacterial activities. *RSC Adv.* **2018**, *8*, 10124–10140. [[CrossRef](#)]
74. Zheng, C.; Yang, H.; Cui, Z.; Zhang, H.; Wang, X. A novel  $Bi_4Ti_3O_{12}/Ag_3PO_4$  heterojunction photocatalyst with enhanced photocatalytic performance. *Nanoscale Res. Lett.* **2017**, *12*, 1–12. [[CrossRef](#)] [[PubMed](#)]
75. Cui, Z.; Yang, H.; Zhao, X. Enhanced photocatalytic performance of g- $C_3N_4/Bi_4Ti_3O_{12}$  heterojunction nanocomposites. *Mater. Sci. Eng. B* **2018**, *229*, 160–172. [[CrossRef](#)]
76. Hummers, W.S., Jr.; Offeman, R.E. Preparation of graphitic oxide. *J. Am. Chem. Soc.* **1958**, *80*, 1339. [[CrossRef](#)]
77. Akbarzadeh, E.; Setayesh, S.R.; Gholami, M.R. Synthesis of the visible-light-driven  $Ag_3VO_4/Ag_3PO_4/Ag$  photocatalysts with enhanced photocatalytic activity. *RSC Adv.* **2016**, *6*, 14909–14915. [[CrossRef](#)]
78. Bagherzadeh, M.; Kaveh, R. A new  $SnS_2$ -BiFeO<sub>3</sub>/reduced graphene oxide photocatalyst with superior photocatalytic capability under visible light irradiation. *J. Photochem. Photobiol. A Chem.* **2018**, *359*, 11–22. [[CrossRef](#)]
79. Bi, Y.; Ouyang, S.; Cao, J.; Ye, J. Facile synthesis of rhombic dodecahedral  $AgX/Ag_3PO_4$  (X= Cl, Br, I) heterocrystals with enhanced photocatalytic properties and stabilities. *Phys. Chem. Chem. Phys.* **2011**, *13*, 10071–10075. [[CrossRef](#)]
80. Tong, H.; Ouyang, S.; Bi, Y.; Umezawa, N.; Oshikiri, M.; Ye, J. Nano-photocatalytic materials: Possibilities and challenges. *Adv. Mater.* **2012**, *24*, 229–251. [[CrossRef](#)]
81. Chen, X.; Dai, Y.; Wang, X. Methods and mechanism for improvement of photocatalytic activity and stability of  $Ag_3PO_4$ : A review. *J. Alloy. Compd.* **2015**, *649*, 910–932. [[CrossRef](#)]
82. Li, G.; Wang, Y.; Mao, L. Recent progress in highly efficient Ag-based visible-light photocatalysts. *RSC Adv.* **2014**, *4*, 53649–53661. [[CrossRef](#)]
83. Yang, Z.-M.; Huang, G.-F.; Huang, W.-Q.; Wei, J.-M.; Yan, X.-G.; Liu, Y.-Y.; Jiao, C.; Wan, Z.; Pan, A. Novel  $Ag_3PO_4/CeO_2$  composite with high efficiency and stability for photocatalytic applications. *J. Mater. Chem. A* **2014**, *2*, 1750–1756. [[CrossRef](#)]
84. Tang, Y.; Jiang, Z.; Xing, G.; Li, A.; Kanhere, P.D.; Zhang, Y.; Sum, T.C.; Li, S.; Chen, X.; Dong, Z. Efficient  $Ag@AgCl$  cubic cage photocatalysts profit from ultrafast plasmon-induced electron transfer processes. *Adv. Funct. Mater.* **2013**, *23*, 2932–2940. [[CrossRef](#)]
85. Wang, D.; Li, Z.; Shang, L.; Liu, J.; Shen, J. Heterostructured  $Ag_3PO_4/TiO_2$  film with high efficiency for degradation of methyl orange under visible light. *Thin Solid Film.* **2014**, *551*, 8–12. [[CrossRef](#)]
86. Cui, X.; Li, Y.; Zhang, Q.; Wang, H. Silver orthophosphate immobilized on flaky layered double hydroxides as the visible-light-driven photocatalysts. *Int. J. Photoenergy* **2012**, *2012*. [[CrossRef](#)]
87. Wang, Q.; Cai, J.; Zhang, L. In situ synthesis of  $Ag_3PO_4$ /cellulose nanocomposites with photocatalytic activities under sunlight. *Cellulose* **2014**, *21*, 3371–3382. [[CrossRef](#)]
88. Wang, W.; Cheng, B.; Yu, J.; Liu, G.; Fan, W. Visible-light photocatalytic activity and deactivation mechanism of  $Ag_3PO_4$  spherical particles. *Chem. Asian J.* **2012**, *7*, 1902–1908. [[CrossRef](#)]
89. Dong, P.; Xi, X.; Hou, G. Typical non- $TiO_2$ -based visible-light photocatalysts. *Semicond. Photocatal. Mater. Mech. Appl.* **2016**. [[CrossRef](#)]
90. Yan, T.; Zhang, H.; Liu, Y.; Guan, W.; Long, J.; Li, W.; You, J. Fabrication of robust  $M/Ag_3PO_4$  (M= Pt, Pd, Au) Schottky-type heterostructures for improved visible-light photocatalysis. *RSC Adv.* **2014**, *4*, 37220–37230. [[CrossRef](#)]
91. Chen, S.; Chen, X.; Jiang, Q.; Yuan, J.; Lin, C.; Shangguan, W. Promotion effect of nickel loaded on CdS for photocatalytic  $H_2$  production in lactic acid solution. *Appl. Surf. Sci.* **2014**, *316*, 590–594. [[CrossRef](#)]

92. Cheng, F.; Liu, W.-S.; Juan, W.; Wang, Y.-K. Research progress of  $\text{Ag}_3\text{PO}_4$ -based photocatalyst: Fundamentals and performance enhancement. *Trans. Nonferrous Met. Soc. China* **2015**, *25*, 112–121.
93. Thiyagarajan, S.; Singh, S.; Bahadur, D. Reusable sunlight activated photocatalyst  $\text{Ag}_3\text{PO}_4$  and its significant antibacterial activity. *Mater. Chem. Phys.* **2016**, *173*, 385–394. [[CrossRef](#)]
94. Carlson, C.; Hussain, S.M.; Schrand, A.M.; Braydich-Stolle, L.K.; Hess, K.L.; Jones, R.L.; Schlager, J.J. Unique cellular interaction of silver nanoparticles: Size-dependent generation of reactive oxygen species. *J. Phys. Chem. B* **2008**, *112*, 13608–13619. [[CrossRef](#)] [[PubMed](#)]
95. Azizi, M.; Sedaghat, S.; Tahvildari, K.; Derakhshi, P.; Ghaemi, A. Synthesis of silver nanoparticles using *Peganum harmala* extract as a green route. *Green Chem. Lett. Rev.* **2017**, *10*, 420–427. [[CrossRef](#)]
96. Harish, R.; Nisha, K.; Prabakaran, S.; Sridevi, B.; Harish, S.; Navaneethan, M.; Ponnusamy, S.; Hayakawa, Y.; Vinniee, C.; Ganesh, M. Cytotoxicity assessment of chitosan coated CdS nanoparticles for bio-imaging applications. *Appl. Surf. Sci.* **2020**, *499*, 143817. [[CrossRef](#)]
97. Majhi, D.; Das, K.; Mishra, A.; Dhiman, R.; Mishra, B. One pot synthesis of  $\text{CdS}/\text{BiOBr}/\text{Bi}_2\text{O}_2\text{CO}_3$ : A novel ternary double Z-scheme heterostructure photocatalyst for efficient degradation of atrazine. *Appl. Catal. B Environ.* **2020**, *260*, 118222. [[CrossRef](#)]
98. Zhang, C.; Wang, J.; Chi, R.; Shi, J.; Yang, Y.; Zhang, X. Reduced graphene oxide loaded with  $\text{MoS}_2$  and  $\text{Ag}_3\text{PO}_4$  nanoparticles/PVA interpenetrating hydrogels for improved mechanical and antibacterial properties. *Mater. Des.* **2019**, *183*, 108166. [[CrossRef](#)]
99. Cao, Y.; Zhang, Y.-H.; Yu, X.-H.; Wang, H.-J. Facile synthesis and antineoplastic activity of bovine serum albumin-conjugated Ag/Ca phosphate nanocomposites. *Micro Nano Lett.* **2012**, *7*, 489–491. [[CrossRef](#)]

**Publisher’s Note:** MDPI stays neutral with regard to jurisdictional claims in published maps and institutional affiliations.



© 2020 by the authors. Licensee MDPI, Basel, Switzerland. This article is an open access article distributed under the terms and conditions of the Creative Commons Attribution (CC BY) license (<http://creativecommons.org/licenses/by/4.0/>).